Canonical approach to cation flux calibration in oxide molecular-beam epitaxy

Jiaxin Sun,[1,*] Christopher T. Parzyck,[2] June H. Lee,[1,†] Charles M. Brooks,[1] Lena F. Kourkoutis,[3,7] Xianglin Ke,[4,‡] Rajiv Misra,[4] Jürgen Schubert,[5] Felix V. Hensling,[1] Matthew R. Barone,[1] Zhe Wang,[1] Megan E. Holtz,[1,3,§] Nathaniel J. Schreiber,[1] Qi Song,[1] Hanjong Paik,[1,6] Tassilo Heeg,[1,∥] David A. Muller,[3,7] Kyle M. Shen,[2,7] and Darrell G. Schlom[1,7,8,¶]

[1]*Department of Materials Sciences and Engineering, Cornell University, Ithaca, New York 14853, USA*
[2]*Department of Physics, Laboratory of Atomic and Solid State Physics, Cornell University, Ithaca, New York 14853, USA*
[3]*School of Applied and Engineering Physics, Cornell University, Ithaca, New York 14853, USA*
[4]*Department of Physics and Materials Research Institute, Pennsylvania State University, University Park, Pennsylvania 16802, USA*
[5]*Peter Grünberg Institute (PGI-9) and JARA-Fundamentals of Future Information Technology, Forschungszentrum Jülich GmbH, 52425 Jülich, Germany*
[6]*Platform for the Accelerated Realization, Analysis, and Discovery of Interface Materials (PARADIM), Cornell University, Ithaca, New York 14853, USA*
[7]*Kavli Institute at Cornell for Nanoscale Science, Ithaca, New York 14853, USA*
[8]*Leibniz-Institut für Kristallzüchtung, Max-Born-Straße 2, 12489 Berlin, Germany*

(Received 28 November 2021; accepted 14 February 2022; published 29 March 2022)

Molecular-beam epitaxy (MBE) is the gold standard for the epitaxial growth of complex oxides with the best material properties as determined by respective figures of merit. Unfortunately, once more than one cation is involved in the material desired, MBE growth often becomes plagued by difficulties in stoichiometry control. Instead of relying on a quartz crystal microbalance to measure the fluxes of the individual molecular beams, which lacks accuracy, or reflection high-energy electron diffraction oscillations of the targeted multication oxide in layer-by-layer growth, which lacks general applicability, here, we describe a canonical approach based on the growth of films of the constituent binary oxides or metals individually for cation flux calibration. This method can calibrate the flux of each molecular beam with an absolute accuracy of ±1%. After describing the growth parameters of binary oxides or metals enabling the individual fluxes of 39 elements of the periodic table to be determined, we demonstrate the efficacy of this approach by applying it to the growth of the quaternary ferromagnetic metal $La_{0.5}Sr_{0.5}CoO_{3-\delta}$ to achieve films with transport properties rivalling the best reported using thin-film growth techniques providing stoichiometric transfer.

DOI: 10.1103/PhysRevMaterials.6.033802

I. INTRODUCTION

Complex oxides are a microcosm of condensed matter physics that host a plethora of fascinating physical phenomena [1,2] such as many-body physics (Sr_2RuO_4, Sr_2RhO_4) [3–6], unconventional superconductivity ($YBa_2Cu_3O_{7-\delta}$, $HgBa_2Ca_2Cu_3O_{8+\delta}$, $Nd_{0.82}Sr_{0.18}NiO_2$) [7–10], ferroelectricity ($PbZr_{0.2}Ti_{0.8}O_3$, $LuFeO_3$) [11,12], complex magnetism ($SrFeO_3$, $BaFe_{12}O_{19}$) [13,14], multiferroicity ($BiFeO_3$, strained $EuTiO_3$) [15,16], insulator-to-metal transitions ($LaCoO_3$, $TmBaMn_2O_6$) [17,18], colossal magnetoresistance ($Pr_{0.7}Ca_{0.3}MnO_3$) [19], high-mobility wide-gap semiconductors ($BaSnO_3$, $ZnGa_2O_4$) [20,21], and much more. In the last few decades, advances in the synthesis sciences of oxide thin films have brought not only platforms to study and control interplays of physical phenomena but also high-performance oxide electronics such as metal-oxide-semiconductor field-effect transistors [22,23] and Josephson junctions [24–26]. Numerous epitaxial growth methods have been successfully adapted and refined for this challenge, including pulsed-laser deposition (PLD) [27,28], magnetron sputtering [29,30], chemical vapor deposition [31,32], and molecular-beam epitaxy (MBE) [33–35]. Owing partly to the ultrahigh vacuum environment, low-energy molecular beams, and the ability to deliver precise, submonolayer doses in layer-by-layer growth, MBE is the gold standard for the epitaxial growth of complex oxides with the best figures of merit of material properties [36]. As an example, the residual resistivity ratio (RRR $= \rho_{300\,K}/\rho_{4\,K}$), which is the ratio of the room-temperature resistivity to the resistivity at 4 K, is one of the most sensitive parameters to imperfections in metallic

*Present address: Lam Research Corporation, 4650 Cushing Parkway, Fremont, California 94538, USA.
†Present address: Neutron Science Division, Korea Atomic Energy Research Institute, Daejeon, Republic of Korea, 34057.
‡Present address: Department of Physics and Astronomy, Michigan State University, East Lansing, Michigan 48824, USA.
§Present address: Department of Metallurgical and Materials Engineering, Colorado School of Mines, Golden, Colorado 80401, USA.
∥Present address: Heeg Vacuum Engineering, 50171 Kerpen, Germany.
¶Author to whom correspondence should be addressed: schlom@cornell.edu

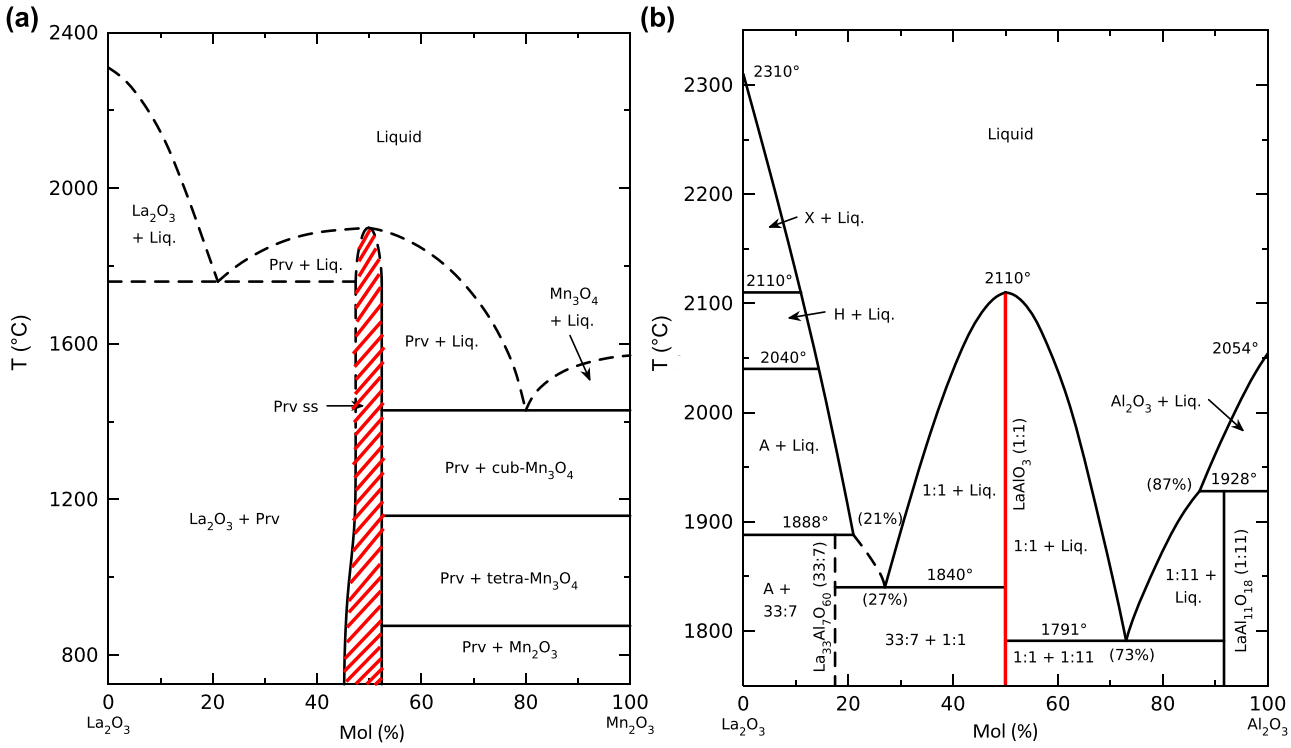

FIG. 1. Bulk binary phase diagrams of (a) La_2O_3-Mn_2O_3 and (b) La_2O_3-Al_2O_3 systems showing significant differences in the stability field (highlighted in red) of the perovskite phase. While $LaAlO_3$ is a line compound with negligible tolerance of off-stoichiometry, $LaMnO_3$ can accommodate up to 10% excess manganese and 20% excess lanthanum while maintaining the single-phase perovskite structure. Note that Prv ss signifies perovskite solid solution. (a) and (b) are reproduced from Refs. [75,76] with permission.

oxides. The RRRs of MBE-grown oxides, namely, $SrVO_3$ and $SrRuO_3$, are the highest among reported thin film studies and even higher than those of single crystals [37–39]. In another example, the unprecedented material purity and perfection in MBE growth is also demonstrated in the observation of the fractional quantum Hall effect in ZnO/MgZnO heterostructures with record carrier mobilities [40].

In addition to superior film properties, there is an important distinction between MBE and other techniques for the epitaxial growth of complex oxides. In PLD and magnetron sputtering, the target materials are typically preoxidized stoichiometric mixtures. Ablation from high-energy beams results in so-called *stoichiometric transfer* where the film retains the same composition as the target [28]. This is, however, only an approximation. Due to factors such as the angular dependence of the species leaving the target and laser fluences, the composition delivered to the film is, in general, not the same as that of the target [41–45]. In contrast to the case of PLD and sputtering, in MBE growth, molecular beams of the constituent species are sublimed/evaporated from individual effusion cells or electron beam sources that each generate a molecular beam of a single-element species. To form oxides containing multiple cations, which is the general case of interest, the fluxes of the molecular beams of the constituent elements need to be independently controlled. In certain cases, the impinging species are volatile where their sticking coefficients depend on growth parameters such as temperature and oxidant pressure. In this case, the volatilities of elemental [46,47], organometallic [35,48–55], and oxide/suboxide species [56–58] can be exploited to realize adsorption-controlled growth, where excess species desorb, enabling a self-limited single-phase deposition regime where automatic composition control is provided by thermodynamics [38,59–69]. In the more general case, however, the fluxes of most if not all molecular beams need to be accurately controlled.

While deliberate deviations from exact stoichiometry have been increasingly explored to introduce defects to engineer the properties of materials [70], off-stoichiometry due to inaccurate flux calibration remains the most prevalent source of undesired defects. Defects related to off-stoichiometry include cation or oxygen vacancies and vacancy clusters, antisite defects, point-defect complexes, and stacking faults. Such defects often degrade the properties of materials. For instance, even slight ruthenium deficiency suppresses superconductivity in Sr_2RuO_4 [71]. Even though the importance of stoichiometry is underscored, it is rather seldom that the dependence of properties on stoichiometry is adequately discussed in the literature [52,72–74].

Different materials have innately different tolerances to off-stoichiometry. To illustrate this point, the binary phase diagrams of $LaMnO_3$ and $LaAlO_3$, which are two similar materials with the perovskite structure, are reproduced in Figs. 1(a) and 1(b), respectively. In bulk form, $LaMnO_3$ can tolerate up to 10% excess manganese ($La_{0.908}MnO_3$ at 850 °C) and up to 20% excess lanthanum ($LaMn_{0.832}O_3$ at 850 °C) and remain a single phase with the perovskite structure. In contrast, $LaAlO_3$ is a line compound where even negligible off-stoichiometry is expelled and results in secondary phases [75,76].

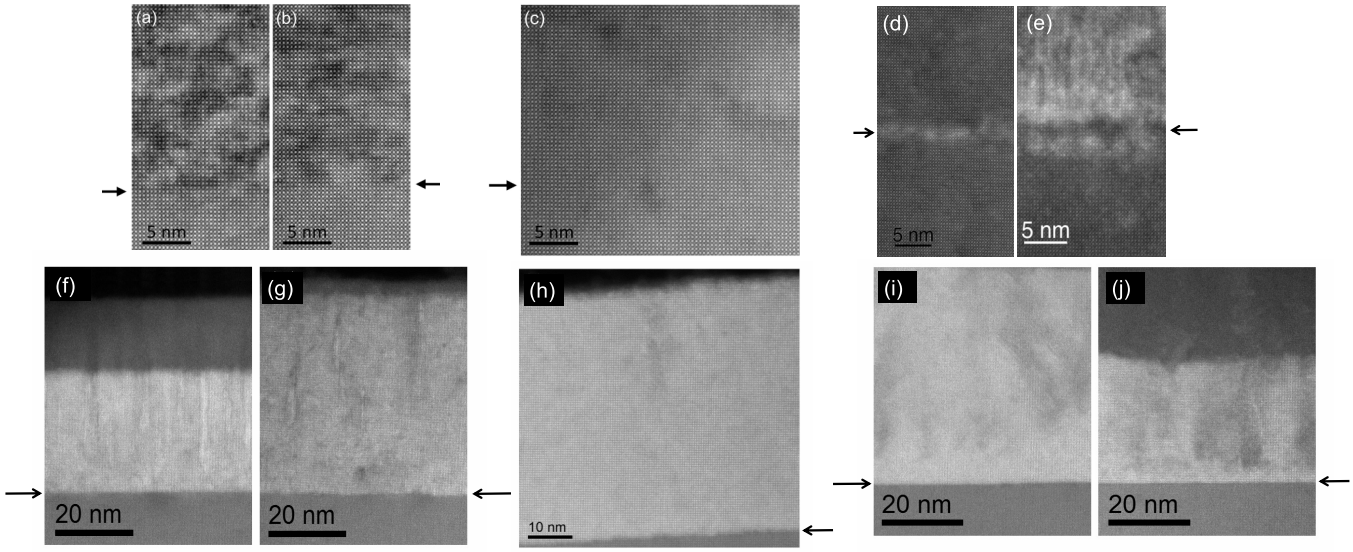

FIG. 2. High-angle annular dark-field scanning transmission electron microscopy (HAADF-STEM) images of stoichiometric and nonstoichiometric $SrTiO_3$ and $EuTiO_3$ films. $Sr_{1+\delta}TiO_x$ with excess titanium: (a) $\delta = -0.20$ and (b) $\delta = -0.09$, (c) stoichiometric $SrTiO_3$, and excess strontium: (d) $\delta = 0.02$ and (e) $\delta = 0.19$. $Eu_{1+\delta}TiO_x$ with excess titanium: (f) $\delta = -0.25$ and (g) $\delta = -0.12$, (h) stoichiometric $EuTiO_3$, and excess europium: (i) $\delta = 0.11$ and (j) $\delta = 0.22$. No obvious secondary impurity phases are observed, and instead, the large deviation in stoichiometry is manifested as point defects (including defect complexes) as observed by graded interfaces and mottled diffraction contrast within the films. (a)–(c) are reprinted from Ref. [81] with permission.

In off-equilibrium epitaxial growth, the nucleation of secondary phases can be further suppressed by kinetic factors arising from a low growth temperature. Such examples include the perovskite titanates $SrTiO_3$ and $EuTiO_3$. In bulk, $SrTiO_3$ is a line compound where even an excess of 0.01% strontium results in $(SrO)_2$ stacking faults [26,77] that mimic the rock-salt layers in the Ruddlesden-Popper homologous series [78–80]. In MBE-grown thin films, however, $SrTiO_3$ and $EuTiO_3$ readily accommodate ∼20% excess titanium or ∼20% excess *A*-site species (Sr/Eu) [81,82] through the formation of point defects when grown at typical growth temperatures ∼650 °C). As shown in the high-angle annular dark-field scanning transmission electron microscopy (HAADF-STEM) images in Fig. 2, no obvious secondary phases are observed in $SrTiO_3$ with excess titanium ($Sr_{1+\delta}TiO_x$ with $\delta < 0$) or excess strontium ($Sr_{1+\delta}TiO_x$ with $\delta > 0$) for $-0.2 < \delta < 0.19$ nor in $EuTiO_3$ with excess titanium ($Eu_{1+\delta}TiO_x$ with $\delta < 0$) or excess europium ($Eu_{1+\delta}TiO_x$ with $\delta > 0$) for $-0.25 < \delta < 0.22$, despite the huge deviations from stoichiometric composition. The off-stoichiometry manifests as point defects, which are evident in the mottled appearance of the film on the atomic scale. Note that no secondary phases are observed by electron microscopy or x-ray diffraction (XRD) in these massively nonstoichiometric films. While changes in lattice constants are observed, as shown in Fig. S1 in the Supplemental Material [83], the films remain fully epitaxial and exhibit XRD peaks with narrow rocking curves [81,82]. The compositional disorder has been frozen in as point defects (and point-defect complexes) by the relatively low growth temperature (compared with the melting temperature) involved.

These examples highlight two important but often overlooked points: (1) just because a film is single phase does not guarantee that the film is stoichiometric, and (2) not all single-phase films have the same ground state if their stoichiometries are different. A powerful example of the latter point is the sensitivity of the antiferromagnetic ground state of single-phase $EuTiO_3$ to nonstoichiometry. Bulk (unstrained) $EuTiO_3$ has an antiferromagnetic ground state at low temperature [84,85], but the energy difference between the ferromagnetic and antiferromagnetic ground states is small [86,87]. Due to point defects associated with nonoptimal laser ablation, $EuTiO_3$ films grown by PLD are weakly ferromagnetic at low temperature [88–91]. By calibrating using Rutherford backscattering spectrometry (RBS) and systematically varying Eu/Ti stoichiometry, we show that precise composition control of $EuTiO_3$ is needed to observe its antiferromagnetic ground state in unstrained films grown by MBE. Even percent level Eu/Ti excess leads to weak ferromagnetism, as shown in the magnetization measurement in Fig. S2 in the Supplemental Material [83].

Given the importance of stoichiometry control, several *in situ* flux measurement techniques have been developed that utilize either an ion gauge (or beam-flux monitor) [92], quartz crystal microbalance (QCM) [93,94], mass spectrometry [95], atomic absorption spectroscopy (AAS) [96], electron impact emission spectroscopy (EIES) [97], or cold cathode emission spectroscopy [98]. Of these, QCM, AAS, and EIES are the most widely utilized today for the growth of oxides by MBE. While a QCM can provide a rough estimate of the flux emanating from each source, it lacks both precision and accuracy. In many MBE systems, the QCM is inserted in front of the substrate heater, i.e., the quartz crystal itself is not in the same location as the substrate. Due in part to the angular dependence of the flux emanating from each source [99], QCM-measured fluxes often exhibit errors in excess of 10%. The use of a collimating tube or a sleeve with a smaller opening on MBE sources to prevent source oxidation under

growth at higher pressures [100–103] can further exacerbate this error. Moreover, the calculation of flux values from the change in the oscillation frequency of a quartz crystal requires knowledge of the mass of the species in the molecular beam, but the background atmosphere and impurities can often complicate this picture. For example, due to the high reactivity of barium, the species that impinge upon the quartz crystal can be any combination of Ba, BaO, $BaCO_3$, and BaO_2 depending on the background pressure of the oxidant employed. Flux measurements by AAS and EIES can be stable and reproducible, but as these methods do not directly measure flux, they require calibration. In short, these methods each have shortcomings that limit their practical implementation. Furthermore, there are currently no commercially available AAS systems free of long-term drift issues.

Another commonly practiced method of calibration is based on the observation of *in situ* reflection high-energy electron diffraction (RHEED) oscillations during either growth by codeposition or shuttered layer-by-layer growth. For shuttered growth, the changes in oscillation amplitude, phase, and beat frequencies in relation to surface stoichiometry have been well documented in perovskites like $SrTiO_3$ [81,104–106]. By observing the oscillations and adjusting the temperature of the effusion cell, source fluxes can be corrected in real time. This method can yield better than $\pm 1\%$ error in both flux values and monolayer dose and has been used to synthesize high-quality films of the $(SrO)(SrTiO_3/BaTiO_3)_n$ Ruddlesden-Popper series (with n as high as 20) [107,108]. While this technique works well for select perovskite systems, it lacks general applicability. For some oxides, the requisite growth mode for RHEED oscillations (atom layer by atom layer) cannot be achieved under the growth conditions accessible in standard MBE systems (e.g., for MgO) [109]. Additionally, some systems require conditions close to the stoichiometric composition to get single-phase growth (e.g., for $La_{0.5}Sr_{0.5}CoO_{3-\delta}$ or $YBa_2Cu_3O_{7-x}$) [110,111].

Depending on how it is desired to grow a multicomponent oxide film by MBE, the flux calibration required can be relative or absolute. When growing multicomponent oxides by codeposition, it is only necessary to get the ratio of the incident fluxes correct to provide a desired incident composition. In this case, only relative calibration is needed, though the growth rate will be unknown. The most challenging case is when it is desired to deposit the incident species in doses corresponding to precise monolayers. This requires absolute calibration. It is insufficient to know the ratio between the fluxes; absolute knowledge of the flux of each molecular beam is needed to know the time necessary to deposit a dose corresponding to a full monolayer.

II. APPROACH

Here, we describe an absolute cation flux calibration strategy for the growth of complex oxides by MBE. It involves calibrating the fluxes of the constituent molecular beams by synthesizing calibration films in the form of thermodynamically stable binary oxides or metals and using *in situ* RHEED oscillations or *ex situ* x-ray reflectivity (XRR) measurements to determine the fluxes of the constituent molecular beams. It has the advantage of generality and accuracy over the aforementioned methods. Further, RHEED and XRR are less costly, faster, and more widely available than techniques that measure chemical composition directly, e.g., RBS, inductively coupled plasma emission spectroscopy, electron probe microanalysis, or x-ray fluorescence.

XRR is widely used to measure the thicknesses of thin films and calibrate growth rates for many deposition techniques, including the deposition of amorphous films [112]. It works well on films that are smooth enough so that clear Kiessig fringes are produced from which the film thickness is calculated [113]. RHEED oscillations during film growth by codeposition are also widely used to calculate the growth rate of epitaxial thin films [114,115]. These oscillations only occur under conditions yielding a periodically varying density of step edges [116,117], a growth mode referred to as *atom layer by atom layer* [118] or *birth and spread* [119]. The method we describe in this paper builds upon these principles by providing growth conditions (growth temperature and oxidant pressure)—on commercially available substrates of specified type and orientation, deposition temperature, and oxidant pressure—that yield smooth calibration films giving rise to clear XRR peaks or RHEED oscillations for 39 elements of the periodic table.

Most MBE-compatible, not-so-toxic elements [120] have at least one binary oxide or metal phase that can be epitaxially grown on a commercially available oxide substrate. Many binary oxides share crystal structures that can be grown on isostructural or crystallographically related substrates. These include oxides with the corundum structure (e.g., Fe_2O_3, Cr_2O_3) on α-Al_2O_3, the rutile structure (e.g., VO_2, RuO_2) on TiO_2, the rock-salt structure (e.g., NiO, CaO) on MgO, the bixbyite/fluorite structure (e.g., In_2O_3, Lu_2O_3) on yttrium-stabilized zirconia (YSZ) as well as the spinel structure (e.g., Mn_3O_4, Co_3O_4) on $MgAl_2O_4$. Out of the 60 not-so-toxic elements that possess binary oxides and metals that are solids at room temperature, we have either experimentally identified or found in the literature the optimal growth conditions and appropriate substrates (with sufficiently small lattice mismatch and other characteristics to grow films of the requisite smoothness for this calibration method to work) for 39 elements. Appropriate growth conditions for the binary oxides/metals of these 39 elements are shown in detail in Table S1 in the Supplemental Material [83]. Except for Nd_2O_3 (see discussion in the Supplemental Material [83]), the growth conditions have been carefully selected such that the growth of a single phase can be maintained throughout the film thickness and that XRR and RHEED oscillations can be readily interpreted to calculate accurate flux values. The 21 remaining elements of the 60 not-so-toxic elements either exhibit sufficiently high volatility (alkali metals, Sb, Bi, and Pb) that they are usually appropriate for adsorption-controlled growth conditions [35,38,49–55,58–63,68,121–130], have binary oxides that are often amorphous (B, Si, and Ge), or have multiple competing low-symmetry polymorphs (Zr, Hf, and Ta). In addition, P, I, Re, Eu, Tb, Ho, and Tm are excluded due to lack of literature reports on epitaxial growths of high-quality P_2O_5, I_2O_5, ReO_3, Eu_2O_3, Tb_2O_3, Ho_2O_3, and Tm_2O_3 thin films. To differentiate the different groups of elements and to highlight the broad applicability of this approach, we have summarized the 39 elements to which we have provided a calibration

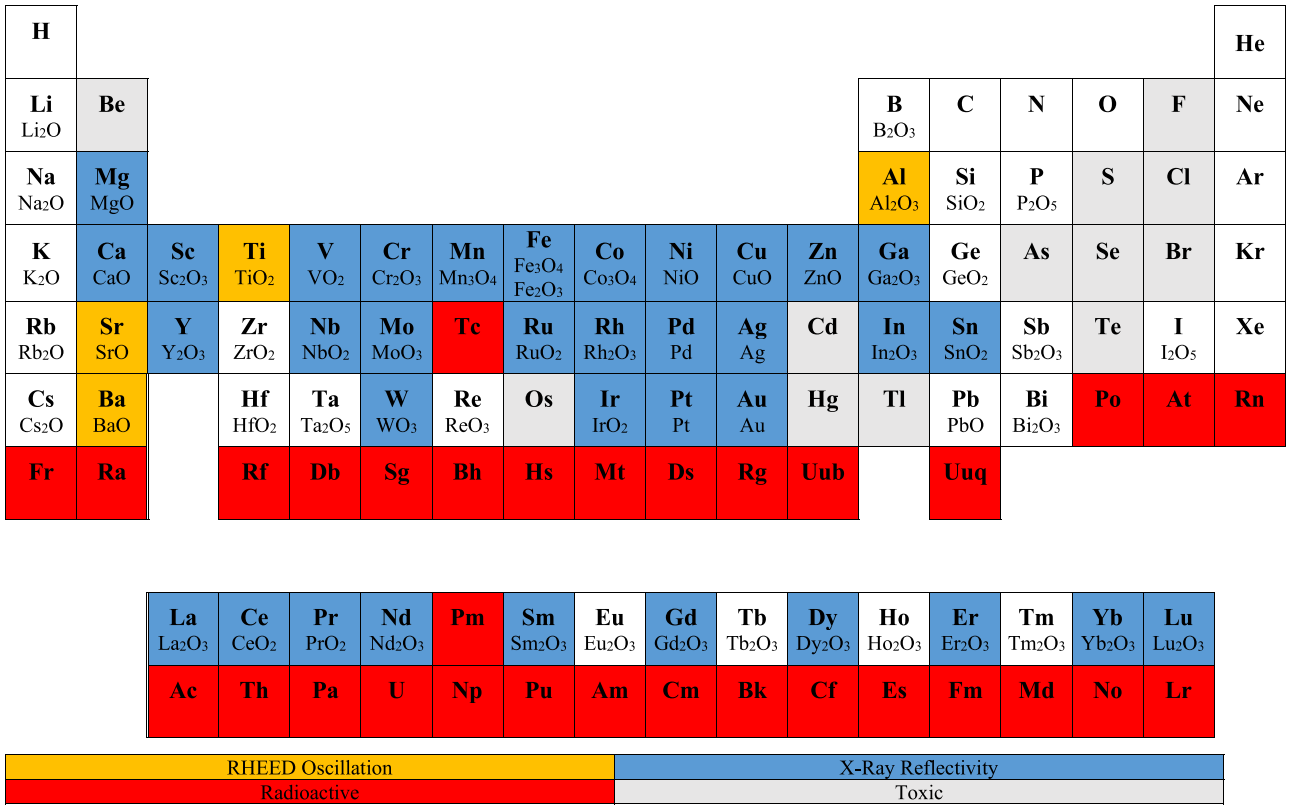

FIG. 3. Periodic table of elements where the metal elements have been grouped to differentiate the means used to determine their fluxes [reflection high-energy electron diffraction (RHEED) oscillations and x-ray reflectivity] for the 60 not-so-toxic elements possessing a binary oxide that is solid at room temperature.

method (RHEED oscillation or XRR) in the periodic table in Fig. 3.

For elements with oxides that can be grown in an atom-layer-by-atom-layer homoepitaxial growth mode on commercially available substrates (e.g., Al_2O_3, TiO_2) or that produce air-sensitive binary oxides (e.g., SrO, BaO) with lattice-matched substrates (typically $<1\%$ biaxial strain), the flux value is best measured by RHEED oscillations. As no shuttering is involved in the growth of these binary oxide calibration layers, the period of each RHEED oscillation corresponds to the smallest charge-neutral formula unit [131]. For elements where the binary oxide or metal films do not exhibit atom-layer-by-atom-layer growth or have large lattice mismatch with the substrate (e.g., CuO, Sc_2O_3), the flux value is best measured by measuring the film thickness by XRR. Here, rather than using the in-plane lattice parameters of the substrate as would be appropriate for a commensurate film, we assume that the film is fully relaxed and use the density of the bulk binary oxide. In doing so, we ignore the defects formed in the film relaxation process as well as thermal strains. In this category, CaO is a special case where the lack of lattice-matched commercial substrate prevents atom-layer-by-atom-layer growth and the air sensitivity necessitates a capping layer with known thickness for the most accurate XRR thickness measurement. Special attention should also be paid to MgO and Nd_2O_3 growths due to the step-flow growth mode and competing structural polymorphs, respectively, which are described in detail in the Supplemental Material [83].

Note that the designations of RHEED oscillations and XRR calibration methods for each element are not mutually exclusive but rather the preferred method to yield the most accurate results. For example, many oxides give RHEED oscillations in heteroepitaxial growths (e.g., rock-salt NiO, bixbyite Lu_2O_3, and rutile SnO_2), but the larger uncertainties in the in-plane areal atomic densities due to varying degrees of film relaxation for a thinner film ($\sim$10 monolayers) in RHEED oscillation calibration mode makes the assumption of constant bulk density less valid in comparison to the XRR calibration mode ($\geqslant$10 nm). For the same binary oxide where both calibration modes are possible, RHEED oscillation calibration gives rises to larger errors in comparison to XRR calibration if the lattice or symmetry mismatches with the substrate are considerable. Nonetheless, there are scenarios where RHEED oscillation periodicities can be advantageous. As an example, once the tooling factor between XRR measured flux and RHEED oscillation periodicity is established, RHEED oscillations can be used for rapid *in situ* recalibration if the number of monolayers deposited are similar.

In comparison with QCM measurement or RHEED oscillation calibration of multicomponent oxides where shuttering of the fluxes is involved, the method described here has two key advantages. First, the individual binary oxide or metal calibration layers are grown in the same geometry and with similar growth conditions (temperature and oxidant pressure) as will be used for the eventual multicomponent oxide, thus eliminating geometric tooling factors. Second, this method is widely applicable, giving rise to nearly inexhaustible combinations

for multicomponent oxides. The main disadvantages are (1) every binary oxide and metal film growth requires a new substrate (though water-soluble layers like SrO and BaO can be washed off and the substrates reused), and (2) the uncertainties in the lattice parameters and densities due to thermal expansion, defects, and residual epitaxial or thermal strain give rise to small errors in flux values under the assumption that the calibration film has the same density as the bulk binary oxide. We estimate the accuracy of the method described to be $\leqslant 1\%$ for binary oxides calibrated by RHEED oscillations (we typically record and analyze a total of 10–20 oscillations) and $\leqslant 2\%$ for binary oxides or metal films calibrated by XRR measurement of film thickness. Note that, in comparison with QCM, such errors are smaller in magnitude and always in the same direction, i.e., the tooling factor is constant. Lastly, it should be emphasized that the binary oxide calibration method detailed here, while a standalone method itself, is complimentary to other flux calibration methods. While the absolute flux values measured by QCM have larger errors, much of this error is due to the QCM not measuring the flux at the same position as that where the substrate is located. The tooling factor describing this geometric difference in location often changes over time. Nonetheless, an approximate tooling factor can be established between the QCM flux values and values obtained through the binary oxide calibration methods, by making a QCM measurement to establish the tooling factor every time binary oxide calibration is performed. These QCM tooling factors can then be used for multiple growths, and the tooling factor can be periodically checked and updated, albeit with lower accuracy than if the binary oxide methods described are utilized for every growth.

To illustrate the calibration procedure and demonstrate its efficacy, we next describe its application to the growth of the quaternary $La_{0.5}Sr_{0.5}CoO_{3-\delta}$, a ferromagnetic metallic oxide on $LaAlO_3$ (100) and $SrTiO_3$ (100) substrates. The structural coherence and transport properties are characterized in detail and are shown to rival the best films grown with growth techniques providing stoichiometric transfer.

III. METHODS

Binary oxide/metal, $La_{0.5}Sr_{0.5}CoO_{3-\delta}$, and $Eu_{1+\delta}TiO_x$ thin films are synthesized in a Veeco Gen10 MBE system. The $Sr_{1+\delta}TiO_x$ samples are synthesized in a Veeco 930 MBE system. The metal and suboxide species [56] are evaporated from Ti Ball™ [132], thermal effusion cells, and Telemark electron beam evaporator systems under ultrahigh vacuum or oxidant atmospheres of molecular oxygen, ∼10% ozone (the direct output of the ASTeX AX8401 ozone generator which is $\sim 10\%O_3 + 90\%O_2$), and distilled ozone ($\sim 80\%O_3 + 20\%O_2$).

Chemomechanically polished MgO (100), $(ZrO_2)_{0.905}(Y_2O_3)_{0.095}$ (hereon referred to as YSZ) (100) and (111), $SrTiO_3$ (100), Al_2O_3 (001) and $(1\bar{1}2)$, $MgAl_2O_4$ (100), TiO_2 (110) and (001), and MgF_2 (110) substrates (CrysTec GmbH) are either used as received or etched and annealed to form atomically flat surfaces with step-and-terrace structures. The surface preparation recipes and resulting atomic force microscopy images (measured using Asylum Cypher Environmental AFM) of treated substrates are shown in Table S2 in the Supplemental Material [83].

The $Sr_{1+\delta}TiO_x$ films, which are ∼100 nm in thickness, are grown on $SrTiO_3$ (100) at a substrate temperature of 650 °C under an atmosphere of 5×10^{-7} Torr of molecular oxygen [81]. The strontium-rich films were grown by codeposition of strontium and titanium where both shutters are open at the same time while the titanium-rich films were grown by shuttered layer-by-layer growth where the strontium and titanium shutters are opened alternatively. The $Eu_{1+\delta}TiO_x$ thin films, which are ∼50 nm in thickness, are grown on $SrTiO_3$ (100) at a substrate temperature of 650 °C under an atmosphere of 3×10^{-8} Torr of molecular oxygen by codeposition of europium and titanium [133].

XRD and XRR measurements were carried out using PANalytical Empyrean and X'Pert Pro MRD diffractometers with Cu $K\alpha_1$ radiation. The raw XRR spectra are analyzed using the PANalytical X'Pert Reflectivity software package where the layer thickness is derived from a fast Fourier transform (FFT) after manually defining the critical angle to account for refractive effects [112]. RHEED patterns were recorded using KSA-400 software and a Staib electron gun operating at 13 kV and a filament current of 1.3–1.6 A. The RHEED oscillations are recorded from the phosphor screen using the KSA-400 software, and the oscillation periodicities can be either counted manually or more accurately derived using an FFT method. The stoichiometries of the $Sr_{1+\delta}TiO_x$ and $Eu_{1+\delta}TiO_x$ thin films are measured using RBS with He^+ ions with an energy of 1.4 MeV. The magnetic properties of the $Eu_{1+\delta}TiO_x$ samples were measured by a superconducting quantum interference device magnetometer (Quantum Design Magnetic Property Measurement System). The samples were cooled under an applied magnetic field of 100 Oe, and the magnetization was measured as the samples were warmed in a magnetic field of 100 Oe. HAADF-STEM was performed using an FEI Tecnai F20-ST microscope operating at 200 keV. The electrical transport properties of $La_{0.5}Sr_{0.5}CoO_{3-\delta}$ films were measured using a Quantum Design Physical Property Measurement System (PPMS).

IV. RESULTS AND DISCUSSIONS

To synthesize epitaxial films of $La_{0.5}Sr_{0.5}CoO_{3-\delta}$, first the individual binary oxides La_2O_3, SrO, and Co_3O_4 are grown on YSZ (111), YSZ (100), and $MgAl_2O_4$ (100) substrates, respectively, according to the conditions given in Table S1 in the Supplemental Material [83]. These conditions are selected by surveying the literature and growing films to confirm that they yield good RHEED oscillations or XRR spectra as needed for accurate calibration of the film thickness, from which an accurate absolute flux of each molecular beam can be extracted. The RHEED patterns, XRD θ-2θ scans, and XRR spectra, which are shown in Fig. 4, indicate that the calibration films are smooth, single phase, and the XRD peak positions correspond to the bulk crystal structures. For SrO the RHEED oscillation, periodicity is established by Fourier transforming the RHEED oscillation. For La_2O_3 and Co_3O_4, the film thicknesses are calculated by Fourier transforming the XRR spectra. From the RHEED oscillations and XRR spectra in Fig. 4, the thicknesses of the calibration films were

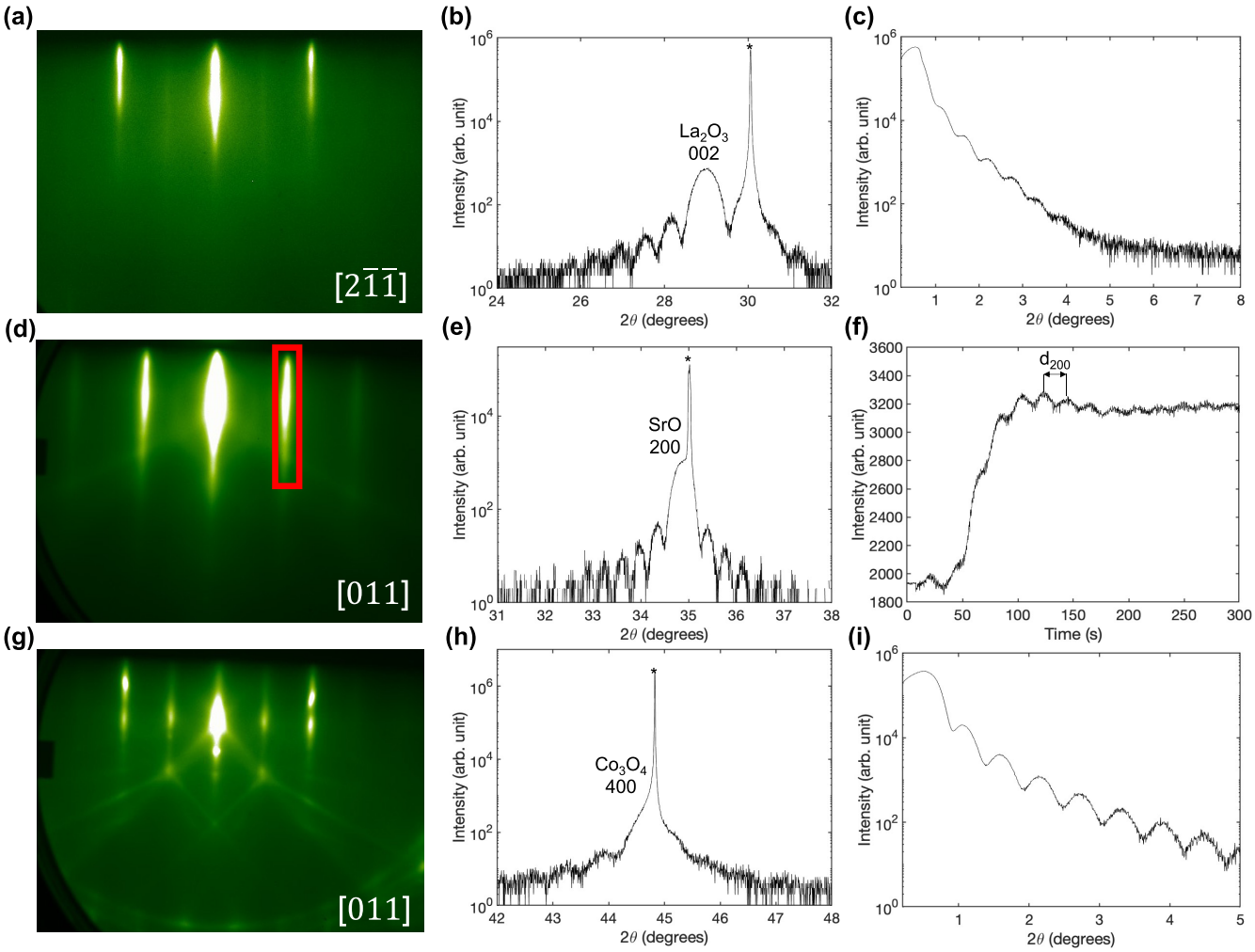

FIG. 4. Flux calibration of the constituent binary oxides of $La_{0.5}Sr_{0.5}CoO_{3-\delta}$. La_2O_3 (a) reflection high-energy electron diffraction (RHEED) pattern along [2$\bar{1}\bar{1}$] of YSZ (111), (b) x-ray diffraction (XRD) θ-2θ scan, and (c) x-ray reflectivity (XRR) spectra. SrO (d) RHEED pattern along [011] of YSZ (100), (e) XRD θ-2θ scans, and (f) RHEED oscillations recorded in the red square of (d), where the period of each oscillation corresponds to half of the distance between the (100) planes of SrO (d_{200}). Co_3O_4 (g) RHEED pattern along [011] of $MgAl_2O_4$ (100), (h) XRD θ-2θ scans, and (i) XRR spectra. The asterisks (*) indicate substrate reflections. Note that to conclusively establish that SrO was the phase grown (and not, for example, SrO_2), the SrO film was capped *in situ* with amorphous TiO_2 before XRD measurements at ambient conditions. From these data, the thicknesses of the calibration films were determined to be 15.6 ± 0.1 nm for La_2O_3, 25.8 ± 0.1 nm for SrO, and 15.2 ± 0.1 nm for Co_3O_4.

determined to be 15.6 ± 0.1 nm for La_2O_3, 25.8 ± 0.1 nm for SrO, and 15.2 ± 0.1 nm for Co_3O_4. The lanthanum, strontium, and cobalt fluxes are then calculated from the derived oscillation periodicity and the film thicknesses using the known lattice parameters of the bulk binary oxides. From the bulk lattice parameters (or alternately known bulk density), the concentration of metal atoms per volume is calculated for each relevant binary oxide or metal in Table S1 in the Supplemental Material [83].

Use of the bulk densities of the binary oxides is an approximation, but as the films are epitaxial and essentially fully dense, it is a reasonable approximation. The validity of the approximation can be considered from two endpoints. For the case of epitaxial growth yielding a fully relaxed film, for example, because the substrate is not well lattice matched, use of the bulk theoretical density is clear, although it does not take film defects into account. The other extreme is a commensurate film that adopts the in-plane lattice constants of the substrate. In this case, the use of the bulk density is equivalent to assuming constant volume (i.e., a Poisson ratio of 0.5) in calculating the out-of-plane lattice constant of the commensurate calibration film.

For this example leading up to the growth of a $La_{0.5}Sr_{0.5}CoO_{3-\delta}$ film, the fluxes are calculated from the data shown in Fig. 4 to be $(2.11 \pm 0.02) \times 10^{13}$ atoms cm^{-2} s^{-1} for lanthanum, $(3.64 \pm 0.02) \times 10^{13}$ atoms cm^{-2} s^{-1} for strontium, and $(2.57 \pm 0.02) \times 10^{13}$ atoms cm^{-2} s^{-1} for cobalt. The accuracy of the fluxes determined are typically $\leqslant$1%. For this method to be effective, it is important that flux drift is minimal since the calibration films from which the fluxes are calculated are grown immediately before the actual film. This calibration process takes several hours to complete

depending on the number of constituents in the complex oxide targeted for growth. For MBE effusion cells, which typically have a flux drift well under 1% per hour, it works well. For sources with higher rates of drift (e.g., a source heated by an electron beam), it is not appropriate.

The generality of this calibration method is demonstrated by the RHEED patterns, XRD scans, and XRR spectra of the other binary oxides/metals shown in Figs. S5–S35 (31 in all), all grown at the conditions suggested in Table S1 in the Supplemental Material [83]. Table S1 in the Supplemental Material [83] also lists the concentration of metal atoms in each of the 39 binary oxides or metals for calculation. Two examples of flux calculations based on RHEED oscillation and XRR used in growth of the $La_{0.5}Sr_{0.5}CoO_{3-\delta}$ film described here are also given in the Supplemental Material [83] through Figs. S3 and S4. For each of the 31 binary oxide or metal calibration growths shown in Figs. S5–S35 in the Supplemental Material [83], the cation flux values used are typically in the range of $5 \times 10^{12} - 5 \times 10^{13}$ atoms cm^{-2} s^{-1}.

The estimated errors in flux calculations based on either RHEED oscillation or XRR for each binary oxide that was grown as parts of this paper are also given in Table S1 in the Supplemental Material [83]. The errors are estimated from the uncertainties in RHEED oscillation periodicities and XRR thicknesses in FFT analyses. While a single range is given for each example, the sources of errors are more complex. For RHEED oscillations, the errors partly come from the uncertainties in the real lattice parameters and mass densities of the epitaxial films at growth conditions. For example, homoepitaxial oscillations (Al_2O_3, TiO_2) are more accurate than heteroepitaxial ones (SrO, BaO) even if the lattice mismatches of the latter are small (<1%). On the other hand, there are errors in simply counting or FFT of oscillations if (1) the oscillations have low signal-to-noise ratios and (2) there are not enough oscillations, which may result from damping. For XRR thicknesses, in addition to the same issue of uncertainties in exact lattice parameters and hence mass densities as discussed above, there are also errors associated with (1) the film roughness and (2) the normalized amplitude of XRR oscillations. As an example of the former, epitaxial Fe_2O_3 is rougher than Fe_3O_4 due to the larger lattice mismatch of Fe_2O_3 grown on Al_2O_3 (001) substrates. The larger surface roughness gives rise to a larger error in the film thickness due to diffuse scattering for the same nominal film thickness. As an example of the latter, the normalized amplitudes of XRR oscillations are weaker for epitaxial systems where the differences of electronic densities between substrate and film are smaller. These errors in XRR thickness estimates can be alleviated by increasing the film thickness, but the effects are twofold. While the number of oscillations increases with increasing film thicknesses, their relative intensities decrease. We therefore recommend that the epitaxial binary oxide/metal films grown for XRR calibrations be at least 10 nm in thickness. The absolute errors in calibration for growth of multicomponent oxides therefore derive from (1) the number of elements involved, (2) the number of RHEED and XRR oscillations counted for each calibration, and (3) the signal-to-noise ratio of each RHEED oscillation and XRR spectrum.

Having established the fluxes of the molecular beams, the $La_{0.5}Sr_{0.5}CoO_{3-\delta}$ film was grown by first heating up the $SrTiO_3$ (100) and $LaAlO_3$ (100) substrates under a background pressure of 1×10^{-6} Torr of distilled ozone to a substrate heater temperature of 600 °C (measured by a thermocouple not in direct contact with the substrate, corresponding to a pyrometer temperature of ∼550 °C). Half-monolayer doses of lanthanum and strontium and integer monolayer doses of cobalt were sequentially deposited on the substrates from thermal effusion cells by pneumatically controlled mechanical shutters following the layered structure of $La_{0.5}Sr_{0.5}CoO_{3-\delta}$ along the [100] growth direction. The RHEED patterns along [011] directions on $SrTiO_3$ (100) and $LaAlO_3$ (100) with sharp diffraction streaks and Kikuchi lines in Figs. 5(a) and 5(b) indicate smooth surfaces with no secondary phases. The XRD θ-2θ scans around the substrate 200 reflection in Figs. 5(c) and 5(d) show shortened and elongated out-of-plane spacings of the $La_{0.5}Sr_{0.5}CoO_{3-\delta}$ film due to tensile and compressive biaxial strains imparted by commensurate growth on the $SrTiO_3$ (100) and $LaAlO_3$ (100) substrates, respectively. Well-defined Laue oscillations indicating excellent smoothness and crystallinity over the full film thickness are also evident. The reciprocal space maps (RSMs) around the (pseudo)-cubic $\bar{1}03$ reflections of $SrTiO_3$ and $LaAlO_3$ are shown, respectively, in Figs. 5(e) and 5(f). Both films are commensurately strained, as is evident from the in-plane component of the film reflections having the same in-plane q vector as the corresponding substrate reflection.

As measured by RSM, the $La_{0.5}Sr_{0.5}CoO_{3-\delta}$ films retain the same structural perfection as the substrates. Structural coherence, however, is a relatively insensitive parameter to stoichiometry in comparison with transport probes. For example, $SrRuO_3$ with up to 30% Ru deficiency can have even better structural coherence than a fully stoichiometric film, but its transport properties are significantly worse and exhibit an upturn in resistivity at low temperature [134]. To gauge the quality of our $La_{0.5}Sr_{0.5}CoO_{3-\delta}$ films calibrated using the methods described, we measured the in-plane longitudinal resistivity (ρ_{xx}) as a function of temperature using four-point contacts in an in-line geometry in a PPMS. Here, ρ_{xx} as a function of temperature for the same 30-nm-thick $La_{0.5}Sr_{0.5}CoO_{3-\delta}$ films grown on $SrTiO_3$ (100) and $LaAlO_3$ (100) substrates are shown in Figs. 6(a) and 6(b), respectively. The room-temperature ρ_{xx}, RRR, and Curie temperature (T_C) are 317 $\mu\Omega$-cm, 2.37, and 200 K on $SrTiO_3$ (100) and 216 $\mu\Omega$-cm, 3.52, and 220 K on $LaAlO_3$ (100). These values all compare favorably with the best epitaxial films grown with stoichiometric transfer techniques reported in the literature [135,136].

The differences in transport characteristics of $La_{0.5}Sr_{0.5}CoO_{3-\delta}$ grown on $SrTiO_3$ (100) and $LaAlO_3$ (100) substrates arise partially from the different strain states. Ordered planes of oxygen vacancies, which have been theorized to accommodate strains [137], have been observed to lie vertically and horizontally with respect to the (001) planes of $SrTiO_3$ and $LaAlO_3$, respectively, in epitaxial $La_{0.5}Sr_{0.5}CoO_{3-\delta}$ films [138]. Such vertically ordered planes of oxygen vacancies structurally distort and affect the in-plane $Co^{3+} - Co^{4+}$ hopping, resulting in additional scattering. The result is an increase in ρ_{xx} and a suppression

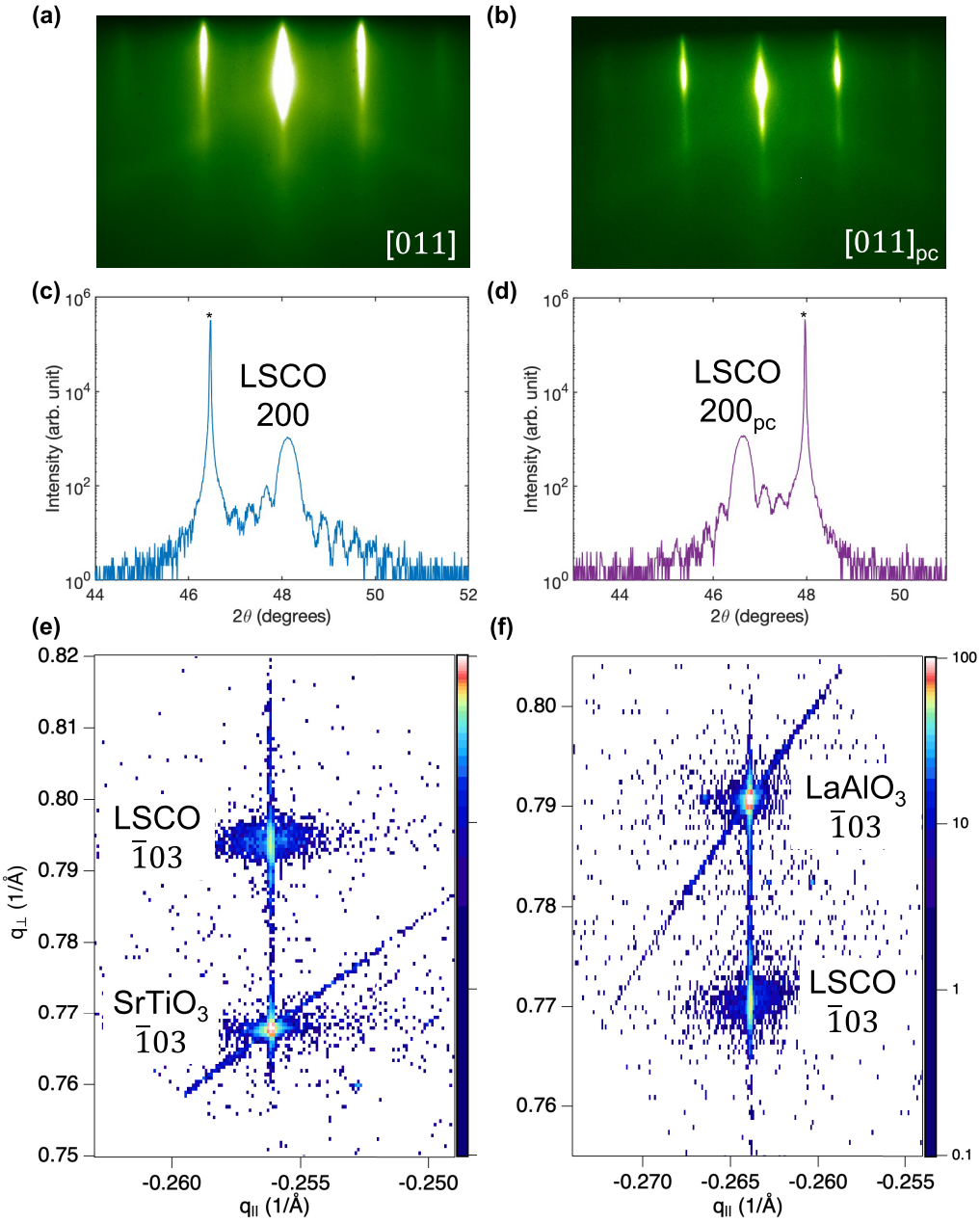

FIG. 5. (a) and (b) Reflection high-energy electron diffraction (RHEED) pattern of 30-nm-thick $La_{0.5}Sr_{0.5}CoO_{3-\delta}$ films grown on $SrTiO_3$ (100) and $LaAlO_3$ (100) along the substrate $[011]_{pc}$ direction. (c) and (d) XRD θ-2θ scans around the 200 film and substrate reflections demonstrating that the $La_{0.5}Sr_{0.5}CoO_{3-\delta}$ films are single phase with smooth interfaces. The asterisks (*) indicate substrate reflections. (e) and (f) reciprocal space map (RSM) around the $\bar{1}03$ film and substrate reflections showing the films are commensurately strained with a clear crystal truncation rod.

in ferromagnetic ordering for epitaxial $La_{0.5}Sr_{0.5}CoO_{3-\delta}$ films on $SrTiO_3$ in comparison with on $LaAlO_3$. Although the room-temperature ρ_{xx} values of epitaxial $La_{0.5}Sr_{0.5}CoO_{3-\delta}$ are low among perovskite oxides, the RRR is significantly smaller than other ternary ferromagnetic metallic oxides such as $SrRuO_3$ [38,39]. The lower RRR is also partially attributed to increased scattering from entropic mixing of $Co^{3+} - Co^{4+}$ in the solid solution network of the B site and that of $La^{3+} - Sr^{2+}$ on the A site [139,140]. The lower RRR has also been reported in other quaternary metallic oxides such as $La_{0.7}Sr_{0.3}MnO_3$ and $La_{0.5}Sr_{0.5}TiO_3$ [141–143]. Although our epitaxial $La_{0.5}Sr_{0.5}CoO_{3-\delta}$ films do not have the highest RRR among all metallic oxides, we stress that the comparatively favorable transport properties of this quaternary oxide demonstrates the general applicability and efficacy of our flux calibration technique.

In addition to the growth of the $La_{0.5}Sr_{0.5}CoO_{3-\delta}$ films reported here, we have also successfully applied this approach to other multicomponent oxide systems including $YBa_2Cu_3O_{7-\delta}/PrBa_2Cu_3O_{7-\delta}/YBa_2Cu_3O_{7-\delta}$ trilayers

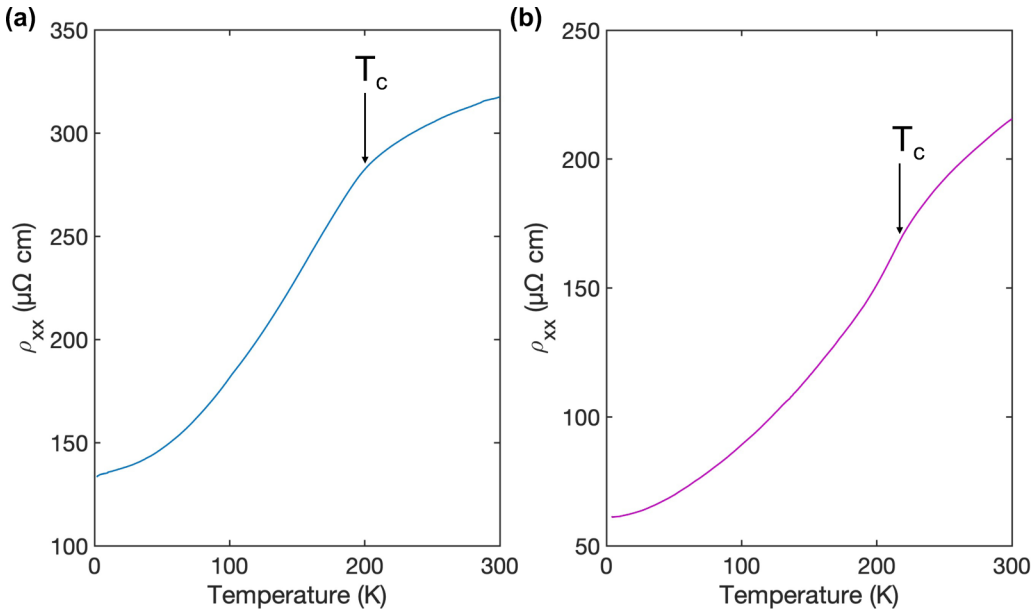

FIG. 6. ρ_{xx} vs temperature of 30-nm-thick $La_{0.5}Sr_{0.5}CoO_{3-\delta}$ grown on (a) $SrTiO_3$ (100) and (b) $LaAlO_3$ (100) substrates. The ferromagnetic T_C values are indicated with black arrows.

of cuprate superconductors [144], the delafossite $PdCoO_2$ [145], the pyrochlore Ce-doped $La_2Sn_2O_7$ [146], as well as spinel solid solutions in the $(Mn, Fe)_3O_4$ system [147]. The successful growths of these complex oxide systems with different crystal structures beyond perovskites demonstrates its broad applicability. Moreover, this approach can be used to synthesize computationally designed, metastable superlattices or heterostructure structures where artificially broken symmetries unleash exotic physical phenomena and exciting materials properties [148,149]. The method we describe could also be readily extended to the growth of multicomponent oxides containing toxic or radioactive elements, e.g., Cd-containing compounds as growth conditions yielding RHEED oscillations of CdO are known [150,151]. Lastly, this method can also be combined appropriately with the aforementioned methods of calibration if even higher precision and accuracy are needed. For example, Pan *et al.* [152,153] used the binary oxide calibration method described as a starting point in the growth of $Nd_{n+1}Ni_nO_{3n+1}$ Ruddlesden-Popper thin films. Finding this calibration alone insufficiently accurate to achieve these challenging phases, they went further and developed a means to make a correction to the initially estimated fluxes by monitoring the RHEED patterns during the shuttered growth of $NdNiO_3$ and, with this more accurate flux calibration, succeeded in the growth of $Nd_{n+1}Ni_nO_{3n+1}$ phases.

In summary, we have described a widely applicable method of cation flux calibration for oxide MBE. The fluxes emanating from each molecular beam are separately determined from RHEED oscillation and XRR measurements on binary oxide and metal thin films. Such accurate, absolute calibration of fluxes is a crucial prerequisite for the growth of more complex oxides by MBE. To demonstrate this method, we have synthesized high-quality quaternary $La_{0.5}Sr_{0.5}CoO_{3-\delta}$ films, the transport properties of which are among the best reported in the literature.

The data that support the findings of this study are available within this paper, Supplemental Material [83], and a data repository [154], including additional data related to the growth and structural characterization. Any additional data connected with the study are available from the corresponding author upon reasonable request.

ACKNOWLEDGMENTS

The authors thank Peter Schiffer and Jacob P. Ruf for their insightful discussions. This paper is primarily supported by Applications and Systems driven Center for Energy-Efficient Integrated NanoTechnologies, one of six centers in the Joint University Microelectronics Program, a Semiconductor Research Corporation program sponsored by the Defense Advanced Research Projects Agency. Material synthesis was performed partly in the Platform for the Accelerated Realization, Analysis, and Discovery of Interface Materials (PARADIM), a user facility supported by the National Science Foundation (NSF) under Cooperative Agreement No. DMR-2039380. This paper made use of the Cornell Center for Materials Research shared facilities, which are supported through the NSF Materials Research Science and Engineering Centers Program (Grant No. DMR-1719875). This paper also made use of the Cornell Energy Systems Institute Shared Facilities partly sponsored by the NSF (Grant No. MRI DMR-1338010) and the Kavli Institute at Cornell. Substrate preparation was performed in part at the Cornell NanoScale Facility, a member of the National Nanotechnology Coordinated Infrastructure, which is supported by the NSF (Grant No. NNCI-2025233). The authors thank Sean C. Palmer for his assistance with substrate preparation.

[1] D. G. Schlom, L. Q. Chen, X. Pan, A. Schmehl, and M. A. Zurbuchen, J. Am. Ceram. Soc. **91**, 2429 (2008).

[2] J. H. Ngai, F. J. Walker, and C. H. Ahn, Annu. Rev. Mater. Res. **44**, 1 (2014).

[3] K. D. Nelson, Z. Q. Mao, Y. Maeno, and Y. Liu, Science **306**, 1151 (2004).

[4] F. Baumberger, N. J. C. Ingle, W. Meevasana, K. M. Shen, D. H. Lu, R. S. Perry, A. P. Mackenzie, Z. Hussain, D. J. Singh, and Z.-X. Shen, Phys. Rev. Lett. **96**, 246402 (2006).

[5] R. S. Perry, F. Baumberger, L. Balicas, N. Kikugawa, N. J. C. Ingle, A. Rost, J. F. Mercure, Y. Maeno, Z. X. Shen, and A. P. Mackenzie, New J. Phys. **8**, 175 (2006).

[6] M. W. Haverkort, I. S. Elfimov, L. H. Tjeng, G. A. Sawatzky, and A. Damascelli, Phys. Rev. Lett. **101**, 026406 (2008).

[7] M. K. Wu, J. R. Ashburn, C. J. Torng, P. H. Hor, R. L. Meng, L. Gao, Z. J. Huang, Y. Q. Wang, and C. W. Chu, Phys. Rev. Lett. **58**, 908 (1987).

[8] H. Maeda, Y. Tanaka, M. Fukutomi, and T. Asano, Jpn. J. Appl. Phys. **27**, L209 (1988).

[9] D. Li, K. Lee, B. Y. Wang, M. Osada, S. Crossley, H. R. Lee, Y. Cui, Y. Hikita, and H. Y. Hwang, Nature (London) **572**, 624 (2019).

[10] A. Schilling, M. Cantoni, J. D. Guo, and H. R. Ott, Nature (London) **363**, 56 (1993).

[11] I. Vrejoiu, G. Le Rhun, L. Pintilie, D. Hesse, M. Alexe, and U. Gösele, Adv. Mater. **18**, 1657 (2006).

[12] E. Magome, C. Moriyoshi, Y. Kuroiwa, A. Masuno, and H. Inoue, Jpn. J. Appl. Phys. **49**, 09ME06 (2010).

[13] S. Ishiwata, T. Nakajima, J.-H. Kim, D. S. Inosov, N. Kanazawa, J. S. White, J. L. Gavilano, R. Georgii, K. M. Seemann, G. Brandl, P. Manuel, D. D. Khalyavin, S. Seki, Y. Tokunaga, M. Kinoshita, Y. W. Long, Y. Kaneko, Y. Taguchi, T. Arima, B. Keimer *et al.*, Phys. Rev. B **101**, 134406 (2020).

[14] S.-P. Shen, Y.-S. Chai, J.-Z. Cong, P.-J. Sun, J. Lu, L.-Q. Yan, S.-G. Wang, and Y. Sun, Phys. Rev. B **90**, 180404(R) (2014).

[15] J. Wang, J. B. Beaton, H. Zheng, V. Nagarajan, S. B. Ogale, B. Liu, D. Viehland, V. Vaithyanathan, D. G. Schlom, U. V. Waghmare, N. A. Spaldin, K. M. Rabe, M. Wuttig, and R. Ramesh, Science **299**, 1719 (2003).

[16] J. H. Lee, L. Fang, E. Vlahos, X. Ke, Y. W. Jung, L. F. Kourkoutis, J. W. Kim, P. J. Ryan, T. Heeg, M. Roeckerath, V. Goian, M. Bernhagen, R. Uecker, P. C. Hammel, K. M. Rabe, S. Kamba, J. Schubert, J. W. Freeland, D. A. Muller, C. J. Fennie *et al.*, Nature (London) **466**, 954 (2010).

[17] T. Nakajima, T. Yamauchi, J. Yamaura, and Y. Ueda, J. Phys. Chem. Solids **67**, 620 (2006).

[18] M. Abbate, J. C. Fuggle, A. Fujimori, L. H. Tjeng, C. T. Chen, R. Potze, G. A. Sawatzky, H. Eisaki, and S. Uchida, Phys. Rev. B **47**, 16124 (1993).

[19] Y. Tomioka, A. Asamitsu, Y. Moritomo, and Y. Tokura, J. Phys. Soc. Japan **64**, 3626 (1995).

[20] H. J. Kim, U. Kim, H. M. Kim, T. H. Kim, H. S. Mun, B.-G. Jeon, K. T. Hong, W.-J. Lee, C. Ju, K. H. Kim, and K. Char, Appl. Phys. Express **5**, 061102 (2012).

[21] Z. Galazka, S. Ganschow, R. Schewski, K. Irmscher, D. Klimm, A. Kwasniewski, M. Pietsch, A. Fiedler, I. Schulze-Jonack, M. Albrecht, T. Schröder, and M. Bickermann, APL Mater. **7**, 022512 (2019).

[22] R. L. Hoffman, B. J. Norris, and J. F. Wager, Appl. Phys. Lett. **82**, 733 (2003).

[23] K. Nomura, H. Ohta, K. Ueda, T. Kamiya, M. Hirano, and H. Hosono, Science **300**, 1269 (2003).

[24] C. T. Rogers, A. Inam, M. S. Hegde, B. Dutta, X. D. Wu, and T. Venkatesan, Appl. Phys. Lett. **55**, 2032 (1989).

[25] K. Char, M. S. Colclough, S. M. Garrison, N. Newman, and G. Zaharchuk, Appl. Phys. Lett. **59**, 733 (1991).

[26] S. Witek, D. M. Smyth, and H. Piclup, J. Am. Ceram. Soc. **67**, 372 (1984).

[27] D. Dijkkamp, T. Venkatesan, X. D. Wu, S. A. Shaheen, N. Jisrawi, Y. H. Min-Lee, W. L. McLean, and M. Croft, Appl. Phys. Lett. **51**, 619 (1987).

[28] D. H. Lowndes, D. B. Geohegan, A. A. Puretzky, D. P. Norton, and C. M. Rouleau, Science **273**, 898 (1996).

[29] C. B. Eom, J. Z. Sun, K. Yamamoto, A. F. Marshall, K. E. Luther, T. H. Geballe, and S. S. Laderman, Appl. Phys. Lett. **55**, 595 (1989).

[30] T. Tybell, C. H. Ahn, and J. M. Triscone, Appl. Phys. Lett. **75**, 856 (1999).

[31] G. J. M. Dormans, P. J. van Veldhoven, and M. de Keijser, J. Cryst. Growth **123**, 537 (1992).

[32] C. M. Foster, Z. Li, M. Buckett, D. Miller, P. M. Baldo, L. E. Rehn, G. R. Bai, D. Guo, H. You, and K. L. Merkle, J. Appl. Phys. **78**, 2607 (1995).

[33] D. G. Schlom, J. N. Eckstein, E. S. Hellman, S. K. Streiffer, J. S. Harris, M. R. Beasley, J. C. Bravman, T. H. Geballe, C. Webb, K. E. von Dessonneck, and F. Turner, Appl. Phys. Lett. **53**, 1660 (1988).

[34] I. Bozovic, J. N. Eckstein, and G. F. Virshup, Phys. C: Supercond. **235–240**, 178 (1994).

[35] B. Jalan, P. Moetakef, and S. Stemmer, Appl. Phys. Lett. **95**, 032906 (2009).

[36] D. G. Schlom, APL Mater. **3**, 062403 (2015).

[37] J. A. Moyer, C. Eaton, and R. Engel-Herbert, Adv. Mater. **25**, 3578 (2013).

[38] H. P. Nair, Y. Liu, J. P. Ruf, N. J. Schreiber, S.-L. Shang, D. J. Baek, B. H. Goodge, L. F. Kourkoutis, Z.-K. Liu, K. M. Shen, and D. G. Schlom, APL Mater. **6**, 046101 (2018).

[39] K. Takiguchi, Y. K. Wakabayashi, H. Irie, Y. Krockenberger, T. Otsuka, H. Sawada, S. A. Nikolaev, H. Das, M. Tanaka, Y. Taniyasu, and H. Yamamoto, Nat. Commun. **11**, 4969 (2020).

[40] J. Falson, D. Maryenko, B. Friess, D. Zhang, Y. Kozuka, A. Tsukazaki, J. H. Smet, and M. Kawasaki, Nat. Phys. **11**, 347 (2015).

[41] T. Venkatesan, X. D. Wu, A. Inam, and J. B. Wachtman, Appl. Phys. Lett. **52**, 1193 (1988).

[42] T. Ohnishi, M. Lippmaa, T. Yamamoto, S. Meguro, and H. Koinuma, Appl. Phys. Lett. **87**, 241919 (2005).

[43] T. Ohnishi, K. Shibuya, T. Yamamoto, and M. Lippmaa, J. Appl. Phys. **103**, 103703 (2008).

[44] T. C. Droubay, L. Qiao, T. C. Kaspar, M. H. Engelhard, V. Shutthanandan, and S. A. Chambers, Appl. Phys. Lett. **97**, 124105 (2010).

[45] R. Dittmann, in *Epitaxial Growth of Complex Metal Oxides*, edited by G. Koster, M. Huijben, and G. Rijnders (Elsevier, Cambridge, 2015), pp. 231–261.

[46] K. G. Günther, Z. Naturforsch. A **13**, 1081 (1958).

[47] H. Freller and K. G. Günther, Thin. Solid. Films **88**, 291 (1982).

[48] W. T. Tsang, Appl. Phys. Lett. **45**, 1234 (1984).
[49] P. Moetakef, J. Y. Zhang, S. Raghavan, A. P. Kajdos, and S. Stemmer, J. Vac. Sci. Technol., A **31**, 041503 (2013).
[50] Y. Matsubara, K. S. Takahashi, Y. Tokura, and M. Kawasaki, Appl. Phys. Express **7**, 125502 (2014).
[51] H.-T. Zhang, L. R. Dedon, L. W. Martin, and R. Engel-Herbert, Appl. Phys. Lett. **106**, 233102 (2015).
[52] R. C. Haislmaier, E. D. Grimley, M. D. Biegalski, J. M. LeBeau, S. Trolier-McKinstry, V. Gopalan, and R. Engel-Herbert, Adv. Funct. Mater. **26**, 7271 (2016).
[53] M. Brahlek, L. Zhang, H.-T. Zhang, J. Lapano, L. R. Dedon, L. W. Martin, and R. Engel-Herbert, Appl. Phys. Lett. **109**, 101903 (2016).
[54] A. Prakash, P. Xu, X. Wu, G. Haugstad, X. Wang, and B. Jalan, J. Mater. Chem. C **5**, 5730 (2017).
[55] T. Wang, L. R. Thoutam, A. Prakash, W. Nunn, G. Haugstad, and B. Jalan, Phys. Rev. Materials **1**, 061601(R) (2017).
[56] K. M. Adkison, S.-L. Shang, B. J. Bocklund, D. Klimm, D. G. Schlom, and Z.-K. Liu, APL Mater. **8**, 081110 (2020).
[57] P. Vogt and O. Bierwagen, Appl. Phys. Lett. **106**, 081910 (2015).
[58] P. Vogt, F. V. E. Hensling, K. Azizie, C. S. Chang, D. Turner, J. Park, J. P. McCandless, H. Paik, B. J. Bocklund, G. Hoffman, O. Bierwagen, D. Jena, H. G. Xing, S. Mou, D. A. Muller, S.-L. Shang, Z.-K. Liu, and D. G. Schlom, APL Mater. **9**, 031101 (2021).
[59] H. Paik, Z. Chen, E. Lochocki, A. Seidner H., A. Verma, N. Tanen, J. Park, M. Uchida, S. Shang, B. Zhou, M. Brützam, R. Uecker, Z. Liu, D. Jena, K. M. Shen, D. A. Muller, and D. G. Schlom, APL Mater. **5**, 116107 (2017).
[60] S. Stoughton, M. Showak, Q. Mao, P. Koirala, D. A. Hillsberry, S. Sallis, L. F. Kourkoutis, K. Nguyen, L. F. J. Piper, D. A. Tenne, N. J. Podraza, D. A. Muller, C. Adamo, and D. G. Schlom, APL Mater. **1**, 042112 (2013).
[61] R. W. Ulbricht, A. Schmehl, T. Heeg, J. Schubert, and D. G. Schlom, Appl. Phys. Lett. **93**, 102105 (2008).
[62] C. D. Theis, J. Yeh, D. G. Schlom, M. E. Hawley, and G. W. Brown, Thin. Solid. Films **325**, 107 (1998).
[63] E. H. Smith, J. F. Ihlefeld, C. A. Heikes, H. Paik, Y. Nie, C. Adamo, T. Heeg, Z.-K. Liu, and D. G. Schlom, Phys. Rev. Materials **1**, 023403 (2017).
[64] R. Heckingbottom, G. J. Davies, and K. A. Prior, Surf. Sci. **132**, 375 (1983).
[65] H. Seki and A. Koukitu, J. Cryst. Growth **78**, 342 (1986).
[66] J. Y. Tsao, J. Cryst. Growth **110**, 595 (1991).
[67] J. Y. Tsao and J. P. Harbison, Phys. Today **46**(10), 125 (1993).
[68] C. M. Brooks, R. Misra, J. A. Mundy, L. A. Zhang, B. S. Holinsworth, K. R. O'Neal, T. Heeg, W. Zander, J. Schubert, J. L. Musfeldt, Z.-K. Liu, D. A. Muller, P. Schiffer, and D. G. Schlom, Appl. Phys. Lett. **101**, 132907 (2012).
[69] J. H. Lee, X. Ke, R. Misra, J. F. Ihlefeld, X. S. Xu, Z. G. Mei, T. Heeg, M. Roeckerath, J. Schubert, Z. K. Liu, J. L. Musfeldt, P. Schiffer, and D. G. Schlom, Appl. Phys. Lett. **96**, 262905 (2010).
[70] A. Dasgupta, S. Saremi, X. Ruijuan, L. R. Dedon, S. Pandya, A. R. Damodaran, and L. W. Martin, J. Mater. Chem. C **6**, 10751 (2018).
[71] G. Kim, Y. E. Suyolcu, J. Herrero-Martin, D. Putzky, H. P. Nair, J. P. Ruf, N. J. Schreiber, C. Dietl, G. Christiani, G. Logvenov, M. Minola, P. A. van Aken, K. M. Shen, D. G. Schlom, and B. Keimer, Phys. Rev. Materials **3**, 094802 (2019).
[72] A. Baki, J. Stöver, T. Schulz, T. Markurt, H. Amari, C. Richter, J. Martin, K. Irmscher, M. Albrecht, and J. Schwarzkopf, Sci. Rep. **11**, 7497 (2021).
[73] M. P. Warusawithana, C. Richter, J. A. Mundy, P. Roy, J. Ludwig, S. Paetel, T. Heeg, A. A. Pawlicki, L. F. Kourkoutis, M. Zheng, M. Lee, B. Mulcahy, W. Zander, Y. Zhu, J. Schubert, J. N. Eckstein, D. A. Muller, C. S. Hellberg, J. Mannhart, and D. G. Schlom, Nat. Commun. **4**, 2351 (2013).
[74] C. Liu, V. F. C. Humbert, T. M. Bretz-Sullivan, G. Wang, D. Hong, F. Wrobel, J. Zhang, J. D. Hoffman, J. E. Pearson, J. S. Jiang, C. Chang, A. Suslov, N. Mason, M. R. Norman, and A. Bhattacharya, Nat. Commun. **11**, 1402 (2020).
[75] J. A. M. van Roosmalen, P. van Vlaanderen, E. H. P. Cordfunke, W. L. IJdo, and D. J. W. IJdo, J. Solid State Chem. **114**, 516 (1995).
[76] P. Wu and A. D. Pelton, J. Alloys Compd. **179**, 259 (1992).
[77] L. J. Knott, N. J. Cockroft, and J. C. Wright, Phys. Rev. B **51**, 5649 (1995).
[78] D. Balz and K. Plieth, Z. Elektrochem. **59**, 545 (1955).
[79] S. N. Ruddlesden and P. Popper, Acta Crystallogr. **10**, 538 (1957).
[80] S. N. Ruddlesden and P. Popper, Acta Crystallogr. **11**, 54 (1958).
[81] C. M. Brooks, L. F. Kourkoutis, T. Heeg, J. Schubert, D. A. Muller, and D. G. Schlom, Appl. Phys. Lett. **94**, 162905 (2009).
[82] C.-H. Lee, V. Skoromets, M. D. Biegalski, S. Lei, R. Haislmaier, M. Bernhagen, R. Uecker, X. Xi, V. Gopalan, X. Martí, S. Kamba, P. Kužel, and D. G. Schlom, Appl. Phys. Lett. **102**, 082905 (2013).
[83] See Supplemental Material at http://link.aps.org/supplemental/10.1103/PhysRevMaterials.6.033802 for structural and magnetic characterization of $EuTiO_3$ and $SrTiO_3$ films, detailed growth conditions of binary oxides and metals and their surface and structural characterizations, sample flux calculations, and atomic force microscopy images of substrates after surface preparation.
[84] T. R. McGuire, M. W. Shafer, R. J. Joenk, H. A. Alperin, and S. J. Pickart, J. Appl. Phys. **37**, 981 (1966).
[85] C.-L. Chien, S. DeBenedetti, and F. D. S. Barros, Phys. Rev. B **10**, 3913 (1974).
[86] P. J. Ryan, J.-W. Kim, T. Birol, P. Thompson, J.-H. Lee, X. Ke, P. S. Normile, E. Karapetrova, P. Schiffer, S. D. Brown, C. J. Fennie, and D. G. Schlom, Nat. Commun. **4**, 1334 (2013).
[87] T. Birol and C. J. Fennie, Phys. Rev. B **88**, 094103 (2013).
[88] K. Kugimiya, K. Fujita, K. Tanaka, and K. Hirao, J. Magn. Magn. Mater. **310**, 2268 (2007).
[89] K. Fujita, N. Wakasugi, S. Murai, Y. Zong, and K. Tanaka, Appl. Phys. Lett. **94**, 062512 (2009).
[90] K. Shimamoto, K. Hatabayashi, Y. Hirose, S. Nakao, T. Fukumura, and T. Hasegawa, Appl. Phys. Lett. **102**, 042902 (2013).
[91] D. Shin, I. Kim, S. Song, Y. Seo, J. Hwang, S. Park, M. Choi, and W. S. Choi, J. Am. Ceram. Soc. **104**, 4606 (2021).
[92] G. R. Giedd and M. H. Perkins, Rev. Sci. Instrum. **31**, 773 (1960).
[93] G. Sauerbrey, Z. Phys. **155**, 206 (1959).

[94] H. K. Pulker and J. P. Decosterd, in *Applications of Piezoelectric Quartz Crystal Microbalances*, edited by C. Lu, and A. W. Czanderna (Elsevier, Amsterdam, 2012), pp. 63–123.

[95] L. L. Chang, L. Esaki, W. E. Howard, and R. Ludeke, J. Vac. Sci. Technol. **10**, 11 (1973).

[96] T. Y. Kometani and W. Wiegmann, J. Vac. Sci. Technol. **12**, 933 (1975).

[97] C. Lu, M. J. Lightner, and C. A. Gogol, J. Vac. Sci. Technol. **14**, 103 (1977).

[98] J. Sakai, G. Chen, K. Hirama, S. Murakami, and T. Ishida, Jpn. J. Appl. Phys. **27**, 319 (1988).

[99] W. Gericke, M. Höricke, and J. von Kalben, Vacuum **42**, 1209 (1991).

[100] I. Bozovic, IEEE Trans. Appl. Supercond. **11**, 2686 (2001).

[101] Y.-S. Kim, N. Bansal, and S. Oh, J. Vac. Sci. Technol., A **29**, 041505 (2011).

[102] Y.-S. Kim, N. Bansal, and S. Oh, J. Vac. Sci. Technol., A **28**, 600 (2010).

[103] P. D. C. King, H. I. Wei, Y. F. Nie, M. Uchida, C. Adamo, S. Zhu, X. He, I. Božović, D. G. Schlom, and K. M. Shen, Nat. Nanotechnol. **9**, 443 (2014).

[104] H. Y. Sun, Z. W. Mao, T. W. Zhang, L. Han, T. T. Zhang, X. B. Cai, X. Guo, Y. F. Li, Y. P. Zang, W. Guo, J. H. Song, D. X. Ji, C. Y. Gu, C. Tang, Z. B. Gu, N. Wang, Y. Zhu, D. G. Schlom, Y. F. Nie, and X. Q. Pan, Nat. Commun. **9**, 2965 (2018).

[105] J. H. Haeni, C. D. Theis, and D. G. Schlom, J. Electroceramics **43**, 385 (2000).

[106] G. Vinai, F. Motti, A. Y. Petrov, V. Polewczyk, V. Bonanni, R. Edla, B. Gobaut, J. Fujii, F. Suran, D. Benedetti, F. Salvador, A. Fondacaro, G. Rossi, G. Panaccione, B. A. Davidson, and P. Torelli, Rev. Sci. Instrum. **91**, 085109 (2020).

[107] N. M. Dawley, E. J. Marksz, A. M. Hagerstrom, G. H. Olsen, M. E. Holtz, V. Goian, C. Kadlec, J. Zhang, X. Lu, J. A. Drisko, R. Uecker, S. Ganschow, C. J. Long, J. C. Booth, S. Kamba, C. J. Fennie, D. A. Muller, N. D. Orloff, and D. G. Schlom, Nat. Mater. **19**, 176 (2020).

[108] M. R. Barone, N. M. Dawley, H. P. Nair, B. H. Goodge, M. E. Holtz, A. Soukiassian, E. E. Fleck, K. Lee, Y. Jia, T. Heeg, R. Gatt, Y. Nie, D. A. Muller, L. F. Kourkoutis, and D. G. Schlom, APL Mater. **9**, 021118 (2021).

[109] M. H. Yang and C. P. Flynn, Phys. Rev. Lett. **62**, 2476 (1989).

[110] V. A. Cherepanov, L. Y. Barkhatova, A. N. Petrov, and V. I. Voronin, ECS Proc. Vol. **1995–1**, 434 (1995).

[111] R. G. Humphreys, N. G. Chew, J. S. Satchell, S. W. Goodyear, J. A. Edwards, and S. E. Blenkinsop, IEEE Trans. Magn. **27**, 1357 (1991).

[112] U. Pietsch, V. Holy, and T. Baumbach, *High-Resolution X-Ray Scattering: From Thin Films to Lateral Nanostructures* (Springer-Verlag, New York, 2004).

[113] H. Kiessig, Ann. Phys. **402**, 769 (1931).

[114] C. E. C. Wood, Surf. Sci. **108**, L441 (1981).

[115] B. A. Joyce, P. J. Dobson, J. H. Neave, K. Woodbridge, J. Zhang, P. K. Larsen, and B. Bôlger, Surf. Sci. **168**, 423 (1986).

[116] J. H. Neave, P. J. Dobson, B. A. Joyce, and J. Zhang, Appl. Phys. Lett. **47**, 100 (1985).

[117] W. Braun, *Applied RHEED: Reflection High-Energy Electron Diffraction during Crystal Growth* (Springer-Verlag, Berlin, Heidelberg, 1999).

[118] E. Bauer, Z. Kristallogr. Cryst. Mater. **110**, 372 (1958).

[119] M. Ohara and R. C. Reid, *Modeling Crystal Growth Rates from Solution* (Prentice-Hall, New Jersey, 1973).

[120] By "not so toxic" we mean that the Occupational Safety and Health Administration (OSHA), part of the United States Department of Labor, has not listed the element or its oxide as having "acute toxicity." The only exception to this in this paper is Ba. Although elemental Ba is not listed by OSHA as having "acute toxicity," BaO is. Occupational Safety and Health Administration, *Standard 1910.1200 App A - Health Hazard Criteria (Mandatory)*, https://www.osha.gov/laws-regs/regulations/standardnumber/1910/1910.1200AppA.

[121] C. D. Theis and D. G. Schlom, J. Cryst. Growth **174**, 473 (1997).

[122] S. Migita, Y. Kasai, H. Ota, and S. Sakai, Appl. Phys. Lett. **71**, 3712 (1997).

[123] C. D. Theis, J. Yeh, D. G. Schlom, M. E. Hawley, G. W. Brown, J. C. Jiang, and X. Q. Pan, Appl. Phys. Lett. **72**, 2817 (1998).

[124] J. Kabelac, S. Ghosh, P. Dobal, and R. Katiyar, J. Vac. Sci. Technol. B **25**, 1049 (2007).

[125] J. F. Ihlefeld, A. Kumar, V. Gopalan, D. G. Schlom, Y. B. Chen, X. Q. Pan, T. Heeg, J. Schubert, X. Ke, P. Schiffer, J. Orenstein, L. W. Martin, Y. H. Chu, and R. Ramesh, Appl. Phys. Lett. **91**, 2005 (2007).

[126] H. P. Nair, J. P. Ruf, N. J. Schreiber, L. Miao, M. L. Grandon, D. J. Baek, B. H. Goodge, J. P. C. Ruff, L. F. Kourkoutis, K. M. Shen, and D. G. Schlom, APL Mater. **6**, 101108 (2018).

[127] M. Uchida, Y. F. Nie, P. D. C. King, C. H. Kim, C. J. Fennie, D. G. Schlom, and K. M. Shen, Phys. Rev. B **90**, 075142 (2014).

[128] Y. F. Nie, P. D. C. King, C. H. Kim, M. Uchida, H. I. Wei, B. D. Faeth, J. P. Ruf, J. P. C. Ruff, L. Xie, X. Pan, C. J. Fennie, D. G. Schlom, and K. M. Shen, Phys. Rev. Lett. **114**, 016401 (2015).

[129] A. B. Mei, L. Miao, M. J. Wahila, G. Khalsa, Z. Wang, M. Barone, N. J. Schreiber, L. E. Noskin, H. Paik, T. E. Tiwald, Q. Zheng, R. T. Haasch, D. G. Sangiovanni, L. F. J. Piper, and D. G. Schlom, Phys. Rev. Materials **3**, 105202 (2019).

[130] Y. Ma, A. Edgeton, H. Paik, B. D. Faeth, C. T. Parzyck, B. Pamuk, S. Shang, Z. Liu, K. M. Shen, D. G. Schlom, and C. Eom, Adv. Mater. **32**, 2000809 (2020).

[131] T. Terashima, Y. Bando, K. Iijima, K. Yamamoto, K. Hirata, K. Hayashi, K. Kamigaki, and H. Terauchi, Phys. Rev. Lett. **65**, 2684 (1990).

[132] C. D. Theis and D. G. Schlom, J. Vac. Sci. Technol. A **14**, 2677 (1996).

[133] J. H. Lee, X. Ke, N. J. Podraza, L. F. Kourkoutis, T. Heeg, M. Roeckerath, J. W. Freeland, C. J. Fennie, J. Schubert, D. A. Muller, P. Schiffer, and D. G. Schlom, Appl. Phys. Lett. **94**, 212509 (2009).

[134] Y. K. Wakabayashi, S. Kaneta-Takada, Y. Krockenberger, K. Takiguchi, S. Ohya, M. Tanaka, Y. Taniyasu, and H. Yamamoto, AIP Adv. **11**, 035226 (2021).

[135] J. Walter, S. Bose, M. Cabero, M. Varela, and C. Leighton, Phys. Rev. Materials **4**, 091401(R) (2020).

[136] R. A. Gunasekaran, J. D. Pedarnig, and M. Dinescu, Appl. Phys. A **69**, 621 (1999).

[137] J. Gazquez, S. Bose, M. Sharma, M. A. Torija, S. J. Pennycook, C. Leighton, and M. Varela, APL Mater. **1**, 012105 (2013).

[138] X. Rui and R. F. Klie, Appl. Phys. Lett. **114**, 233101 (2019).

[139] N. Kikugawa, A. P. Mackenzie, C. Bergemann, R. A. Borzi, S. A. Grigera, and Y. Maeno, Phys. Rev. B **70**, 060508(R) (2004).
[140] N. Kikugawa, A. Peter Mackenzie, and Y. Maeno, J. Phys. Soc. Japan **72**, 237 (2003).
[141] W. Wu, F. Lu, K. H. Wong, G. Pang, C. L. Choy, and Y. Zhang, J. Appl. Phys. **88**, 700 (2000).
[142] R. Shiozaki, K. Takenaka, Y. Sawaki, and S. Sugai, Phys. Rev. B **63**, 184419 (2001).
[143] C. Adamo, X. Ke, H. Q. Wang, H. L. Xin, T. Heeg, M. E. Hawley, W. Zander, J. Schubert, P. Schiffer, D. A. Muller, L. Maritato, and D. G. Schlom, Appl. Phys. Lett. **95**, 112504 (2009).
[144] Y. E. Suyolcu, J. Sun, B. H. Goodge, J. Park, J. Schubert, L. F. Kourkoutis, and D. G. Schlom, APL Mater. **9**, 021117 (2021).
[145] J. Sun, M. R. Barone, C. S. Chang, M. E. Holtz, H. Paik, J. Schubert, D. A. Muller, and D. G. Schlom, APL Mater. **7**, 121112 (2019).
[146] F. V. E. Hensling, D. Dahliah, P. Dulal, P. Singleton, J. Sun, J. Schubert, H. Paik, I. Subedi, B. Subedi, G.-M. Rignanese, N. J. Podraza, G. Hautier, and D. G. Schlom, APL Mater. **9**, 051113 (2021).
[147] A. Bhargava, R. Eppstein, J. Sun, M. A. Smeaton, H. Paik, L. F. Kourkoutis, D. G. Schlom, M. Caspary Toroker, and R. D. Robinson, Adv. Mater. **32**, 2004490 (2020).
[148] E. J. Monkman, C. Adamo, J. A. Mundy, D. E. Shai, J. W. Harter, D. Shen, B. Burganov, D. A. Muller, D. G. Schlom, and K. M. Shen, Nat. Mater. **11**, 855 (2012).
[149] J. A. Mundy, C. M. Brooks, M. E. Holtz, J. A. Moyer, H. Das, A. F. Rébola, J. T. Heron, J. D. Clarkson, S. M. Disseler, Z. Liu, A. Farhan, R. Held, R. Hovden, E. Padgett, Q. Mao, H. Paik, R. Misra, L. F. Kourkoutis, E. Arenholz, A. Scholl *et al.*, Nature (London) **537**, 523 (2016).
[150] E. Sachet, C. T. Shelton, J. S. Harris, B. E. Gaddy, D. L. Irving, S. Curtarolo, B. F. Donovan, P. E. Hopkins, P. A. Sharma, A. L. Sharma, J. Ihlefeld, S. Franzen, and J.-P. Maria, Nat. Mater. **14**, 414 (2015).
[151] E. D. Grimley, A. P. Wynn, K. P. Kelley, E. Sachet, J. S. Dean, C. L. Freeman, J.-P. Maria, and J. M. LeBeau, J. Appl. Phys. **124**, 205302 (2018).
[152] G. A. Pan, D. Ferenc Segedin, H. LaBollita, Q. Song, E. M. Nica, B. H. Goodge, A. T. Pierce, S. Doyle, S. Novakov, D. Córdova Carrizales, A. T. N'Diaye, P. Shafer, H. Paik, J. T. Heron, J. A. Mason, A. Yacoby, L. F. Kourkoutis, O. Erten, C. M. Brooks, A. S. Botana *et al.*, Nat. Mater. **21**, 160 (2022).
[153] G. A. Pan, Q. Song, D. Ferenc Segedin, H. El-Sherif, M.-C. Jung, E. E. Fleck, B. H. Goodge, S. Doyle, D. Córdova Carrizales, A. T. N'Diaye, P. Shafer, H. Paik, L. F. Kourkoutis, A. S. Botana, I. El Baggari, C. M. Brooks, and J. A. Mundy, Electronic properties of $Nd_{n+1}Ni_nO_{3n+1}$ Ruddlesden-Popper nickelate thin films (unpublished).
[154] A repository at https://doi.org/10.34863/802t-xs70 contains detailed growth parameters, as well as RHEED and XRD characterization data, for the samples prepared and measured in the course of this investigation.

Canonical approach to cation flux calibration in oxide molecular-beam epitaxy

Jiaxin Sun,[1,a] Christopher T. Parzyck,[2] June H. Lee,[1,b] Charles M. Brooks,[1] Lena F. Kourkoutis,[3,7] Xianglin Ke,[4,c] Rajiv Misra,[4] Jürgen Schubert,[5] Felix V. Hensling,[1] Matthew R. Barone,[1] Zhe Wang,[1] Megan E. Holtz,[1,3,d] Nathaniel J. Schreiber,[1] Qi Song,[1] Hanjong Paik,[1,6] Tassilo Heeg,[1] David A. Muller,[3,7] Kyle M. Shen,[2,7] and Darrell G. Schlom[1,7,8,*]

1. Department of Materials Sciences and Engineering, Cornell University, Ithaca, New York 14853, USA
2. Department of Physics, Laboratory of Atomic and Solid State Physics, Cornell University, Ithaca, New York 14853, USA
3. School of Applied and Engineering Physics, Cornell University, Ithaca, New York 14854, USA
4. Department of Physics and Materials Research Institute, Pennsylvania State University, University Park, Pennsylvania 16802, USA
5. Peter Grünberg Institute (PGI-9) and JARA-Fundamentals of Future Information Technology, Forschungszentrum Jülich GmbH, 52425 Jülich, Germany
6. Platform for the Accelerated Realization, Analysis, and Discovery of Interface Materials (PARADIM), Cornell University, Ithaca, New York 14853, USA
7. Kavli Institute at Cornell for Nanoscale Science, Ithaca, New York 14853, USA
8. Leibniz-Institut für Kristallzüchtung, Max-Born-Straße 2, 12489 Berlin, Germany

a. Current Address: Lam Research Corporation, 4650 Cushing Parkway, Fremont, California 94538, USA
b. Current Address: Neutron Science Division, Korea Atomic Energy Research Institute, Daejeon, Republic of Korea, 34057
c. Current Address: Department of Physics and Astronomy, Michigan State University, East Lansing, Michigan 48824, USA
d. Current Address: Department of Metallurgical and Materials Engineering, Colorado School of Mines, Golden, Colorado 80401, USA

*. Author to whom correspondence should be addressed: schlom@cornell.edu

Supplementary Material

Out-of-plane lattice constants of $EuTi_{1+\delta}O_x$ and $SrTi_{1+\delta}O_x$

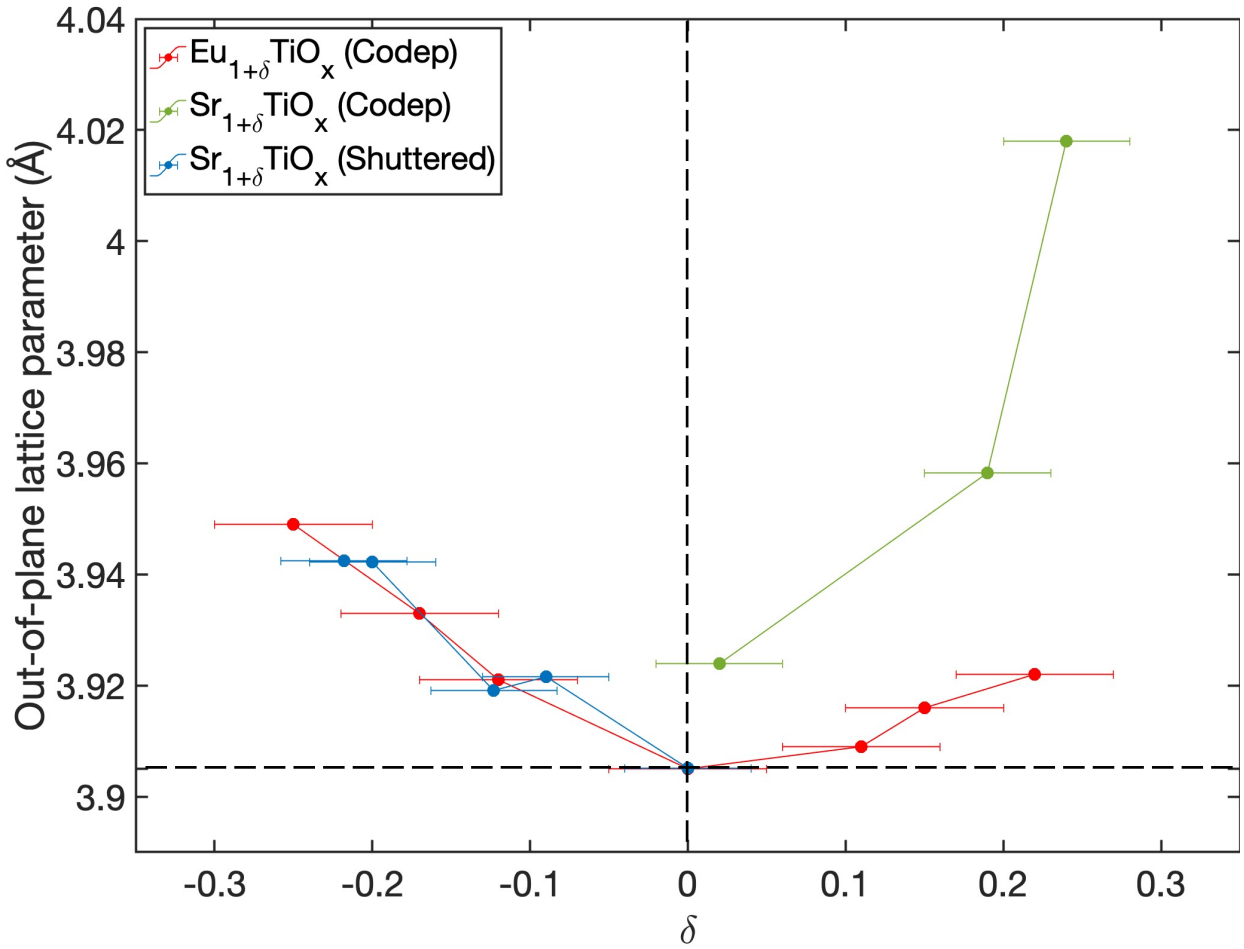

FIG. S1. Comparison of the out-of-plane lattice constants of $EuTiO_3$ and $SrTiO_3$ as a function of europium/strontium excess. The data for off-stoichiometric $SrTiO_3$ films are from Ref. [1]. The vertical dashed line marks the stoichiometric film (δ=0).

Magnetization measurements of $Eu_{1+\delta}TiO_x$ films

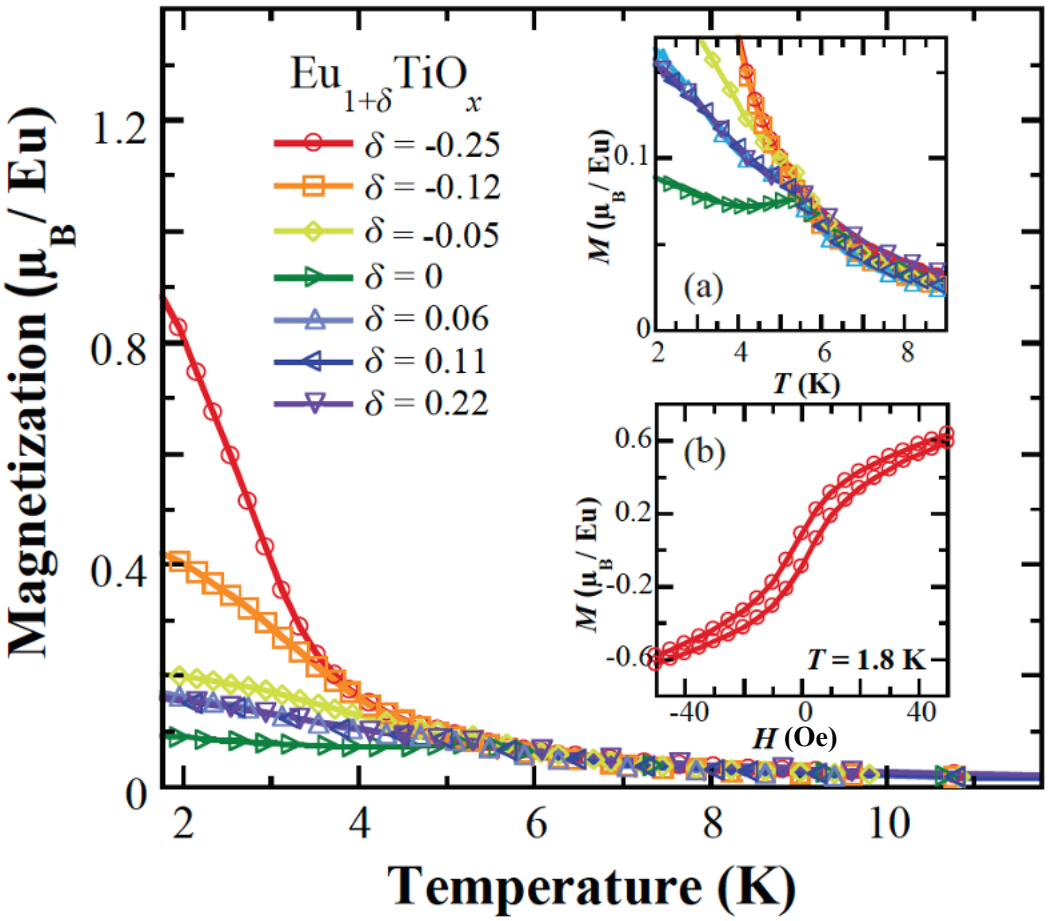

FIG. S2. Field-cooled magnetization of the $Eu_{1+\delta}TiO_x$ films at H=100 Oe. (a) Plotted at small magnetization to make the antiferromagnetic ordering at T_N=5.3 K apparent for the stoichiometric film. (b) The $Eu_{0.75}TiO_x$ film exhibits weak ferromagnetic hysteresis.

Binary oxide/metal thin film growth conditions

TABLE S1. Epitaxial relationship, strain, growth temperature and oxidant pressure for the growth of binary oxide/metal epitaxial thin films

Binary oxide/Metal	Substrate	In-plane Epitaxial Relationship	In-plane Lattice Mismatch (%)	Temperature (°C)	Pressure (Torr)	Atomic Density of Cations (atoms/cm^3)	Estimated Error (%)	Ref
$(1\bar{1}2)$ Al_2O_3	$(1\bar{1}2)$ Al_2O_3	$[110]\|\|[110]$ $[\bar{1}11]\|\|[\bar{1}11]$	0.00 0.00	400	1×10^{-6} O_3	4.69×10^{22}	≤1	[2]
(100) Ag	(100) MgO	[001] || [001]	3.21	25-200	UHV	5.86×10^{22}	N/A	[3]
(100) Au	(100) MgO	[001] || [001]	3.59	100-200	UHV	5.93×10^{22}	N/A	[3]
(100) BaO	(100) $SrTiO_3$	[011] || [001]	-0.30	500	1×10^{-6} O_2/O_3	2.38×10^{22}	≤1	[4]
(100) CaO	(100) MgO	[001] || [001]	-12.4	800	1×10^{-6} O_2/O_3	3.58×10^{22}	≤2	[5]
(111) CeO_2	(111) YSZ	$[10\bar{1}]\|\|[10\bar{1}]$	-5.03	700-900	1×10^{-6} O_3	2.52×10^{22}	≤1	
(100) Co_3O_4	(100) $MgAl_2O_4$	[001] || [001]	0.11	350	1×10^{-6} O_3	4.57×10^{22}	≤1	
(001) Cr_2O_3	(001) Al_2O_3	[100] || [100]	-4.10	480	1×10^{-6} O_3	4.15×10^{22}	≤1	[6,7]
(111) CuO	(100) MgO	$[\bar{1}10]\|\|[011]$	1.00	RT	1×10^{-6} O_3	4.93×10^{22}	≤1	[8]
(111) Dy_2O_3	(111) YSZ	$[1\bar{1}0]\|\|[1\bar{1}0]$	-3.29	700-900	1×10^{-6} O_3	2.66×10^{22}	≤1	
(111) Er_2O_3	(111) Si	$[\bar{1}10]\|\|[\bar{1}01]$	2.95	750	~3.9×10^{-6} O_2	2.73×10^{22}	N/A	[9,10]
(100) Fe_3O_4	(100) MgO	[001] || [001]	0.48	350	1×10^{-6} O_2	4.06×10^{22}	≤1	[11]
(001) Fe_2O_3	(001) Al_2O_3	[100] || [100]	-5.53	480	1×10^{-6} O_3	3.96×10^{22}	≤1	[12]
$(\bar{2}01)$ β-Ga_2O_3	(001) Al_2O_3	$[010]\|\|[1\bar{1}0]$ $[102]\|\|[110]$	6.02 15.0	700	1×10^{-6} O_3	3.82×10^{22}	≤2	[13,14]
(111) Gd_2O_3	(111) Si	$[\bar{1}10]\|\|[\bar{1}01]$	0.41	750	~3.9×10^{-6} O_2	2.53×10^{22}	N/A	[9,10]
(111) In_2O_3	(001) Al_2O_3	$[1\bar{1}0]\|\|[100]$	-13.2	900	1×10^{-6} O_3	3.09×10^{22}	≤1	[15]
(100) In_2O_3	(100) YSZ	[001] || [001]	1.61	600-700	O*	3.09×10^{22}		[16]
(110) IrO_2	(110) TiO_2	[001] || [001] $[\bar{1}10]\|\|[\bar{1}10]$	-6.32 1.98	300	1×10^{-6} O_3	3.12×10^{22}	≤1	[17]
(001) La_2O_3	(111) YSZ	$[100]\|\|[10\bar{1}]$	-7.67	950	1×10^{-6} O_3	2.43×10^{22}	≤1	
(111) Lu_2O_3	(111) YSZ	$[1\bar{1}0]\|\|[1\bar{1}0]$	-1.18	700-900	1×10^{-6} O_3	2.84×10^{22}	≤1	
(100) MgO	(100) MgO	[001] || [001]	0.00	0-500	1×10^{-6} O_2/O_3	5.33×10^{22}	≤1	[18]
(001) Mn_3O_4	(100) $MgAl_2O_4$	[110] || [001]	-0.89	350	1×10^{-6} O_3	3.84×10^{22}	≤1	[19]
(010) MoO_3	(100) $SrTiO_3$	[100] || [001]	-1.46	400-450	O*	1.97×10^{22}	N/A	[20]
(110) NbO_2	(110) MgF_2	[001] || [001] $[\bar{1}10]\|\|[\bar{1}10]$	0.67 -4.64	425	UHV from suboxide source	2.81×10^{22}	≤1	[21]
(001) Nd_2O_3	(111) YSZ	[100] || [100]	-5.08	950	1×10^{-6} O_3	2.62×10^{22}	≤1	
(100) NiO	(100) MgO	[001] || [001]	0.93	400	1×10^{-6} O_3	5.48×10^{22}	≤1	
(111) Pd	(111) YSZ	$[10\bar{1}]\|\|[10\bar{1}]$	32.2	RT	UHV	6.79×10^{22}	≤1	

(111) PrO_2	(111) YSZ	$[10\bar{1}]$ || $[10\bar{1}]$	-4.71	700-900	1×10^{-6} O_3	2.55×10^{22}	≤2	
(111) Pt	(001) Al_2O_3	$[10\bar{1}]$ || [100]	-14.3	550-700	UHV	6.62×10^{22}	≤1	
(001) Rh_2O_3	(001) Al_2O_3	[100] || [100]	-6.97	500	1×10^{-5} O_3	1.90×10^{22}	≤1	[12]
(110) RuO_2	(110) TiO_2	[001] || [001] $[\bar{1}10]$ || $[\bar{1}10]$	-4.70 2.34	300	1×10^{-6} O_3	3.19×10^{22}	≤1	[22]
(111) Sc_2O_3	(111) YSZ	$[1\bar{1}0]$ || $[1\bar{1}0]$	4.53	700-900	1×10^{-6} O_3	3.36×10^{22}	≤1	
(001) Sm_2O_3	(111) YSZ	[100] || [100]	-3.77	900	$1x10^{-6}$ O_3	$2.72x10^{22}$	≤1	
(110) SnO_2	(110) TiO_2	[001] || [001] $[\bar{1}10]$ || $[\bar{1}10]$	-7.14 -3.05	300	1×10^{-6} O_3	2.80×10^{22}	≤1	[23]
(100) SrO	(100) YSZ	[001] || [001]	-0.91	500	1×10^{-6} O_2/O_3	2.91×10^{22}	≤1	
(110) TiO_2	(110) TiO_2	[001] || [001] $[\bar{1}10]$ || $[\bar{1}10]$	0.00 0.00	300	1×10^{-6} O_2/O_3	3.21×10^{22}	≤1	[24]
(110) VO_2	(110) TiO_2	[001] || [001] $[\bar{1}10]$ || $[\bar{1}10]$	3.47 0.83	250-350	1×10^{-6} O_3/O*	3.37×10^{22}	≤2	[25]
$(001)_{pc}$ WO_3	(100) LSAT	$[110]_{pc}$ || [001]	-4.20	600	O*	~1.89×10^{22} (competing polymorphs)	N/A	[26,27] [28,29]
(111) Y_2O_3	(111) YSZ	$[1\bar{1}0]$ || $[1\bar{1}0]$	-3.06	700-900	1×10^{-6} O_3	2.68×10^{22}	≤1	
(111) Yb_2O_3	(001) Al_2O_3	$[1\bar{1}0]$ || [100]	11.67	400	1×10^{-4} O_3	2.68×10^{22}	≤1	[30]
(001) ZnO	(001) Al_2O_3	[110]|| $[1\bar{1}0]$ $[1\bar{1}0]$|| [110]	-18.7 7.57	450-750	1×10^{-6} O_3	4.20×10^{22}	N/A	[31]

UHV – Ultra-high vacuum with background pressure equal to or lower than 1×10^{-8} Torr
RT – Room temperature (<100 °C)
YSZ – Yttrium stabilized zirconia, $(ZrO_2)_{0.905}(Y_2O_3)_{0.095}$
LSAT – $(LaAlO_3)_{0.3}$-$(SrAl_{0.5}Ta_{0.5}O_3)_{0.7}$
O* denotes oxygen plasma/activated oxygen
O_3 denotes either 10% or 80% O_3 with the rest being O_2
O_2/O_3 denotes that either pure O_2, 10% O_3, or 80% O_3 may be used
N/A – No available data

Example Calculations

Co_3O_4 – X-ray Reflectivity

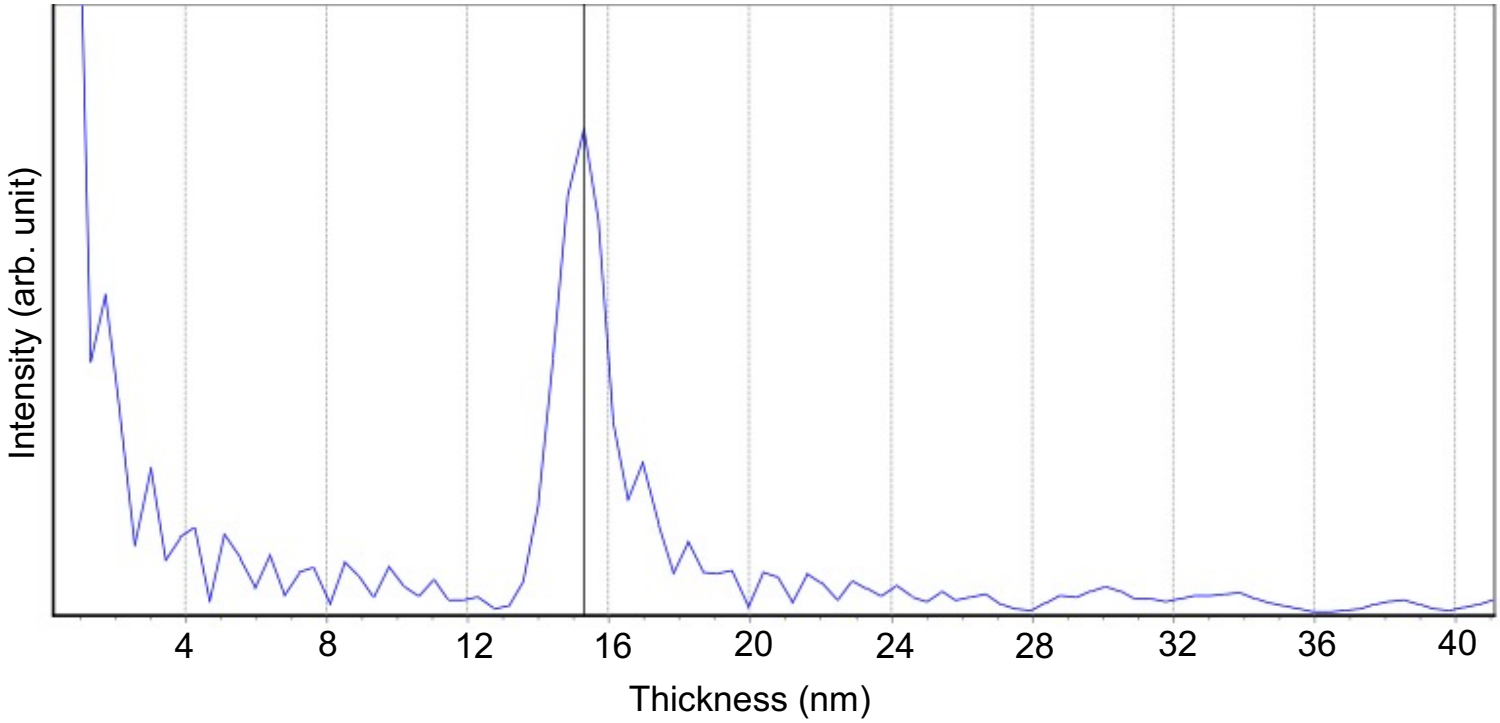

FIG. S3. FFT of Co_3O_4 XRR (shown in Fig. 4(i)) from PANalytical X'Pert Reflectivity software giving an average film thickness of 15.2 ± 0.1 nm.

The FFT of the Co_3O_4 XRR (Fig. 4(i)) from PANalytical X'Pert Reflectivity is shown in Fig. S3 above. It gives an estimated film thickness of 15.2 ± 0.1 nm. Given that the total growth time is 45 minutes and that the density of cobalt atoms in Co_3O_4 is 4.57×10^{22} atoms/cm^3, the Co flux is calculated to be

$$\text{Co flux} = \frac{4.57\times10^{22}\ \text{atoms}/\text{cm}^3 \times (15.2 \pm 0.1)\ \text{nm}}{45\ \text{min}} = (2.57 \pm 0.02)\times10^{13}\ \frac{\text{atoms}}{\text{cm}^2\text{s}}$$

Assuming that the $La_{0.5}Sr_{0.5}CoO_{3-\delta}$ film is commensurately strained to $LaAlO_3$ (100), for an in-plane lattice pseudo-cubic lattice parameter of 3.794 Å, the shutter time for 1 monolayer of CoO_2 is calculated to be

$$\text{Co shutter time} = \frac{\frac{1}{(3.794\times10^{-8})^2}\ \frac{\text{atoms}}{\text{cm}^2}}{(2.57 \pm 0.02)\times10^{13}\ \frac{\text{atoms}}{\text{cm}^2\text{s}}} = 27.0 \pm 0.2\ \text{s}$$

SrO – RHEED oscillation

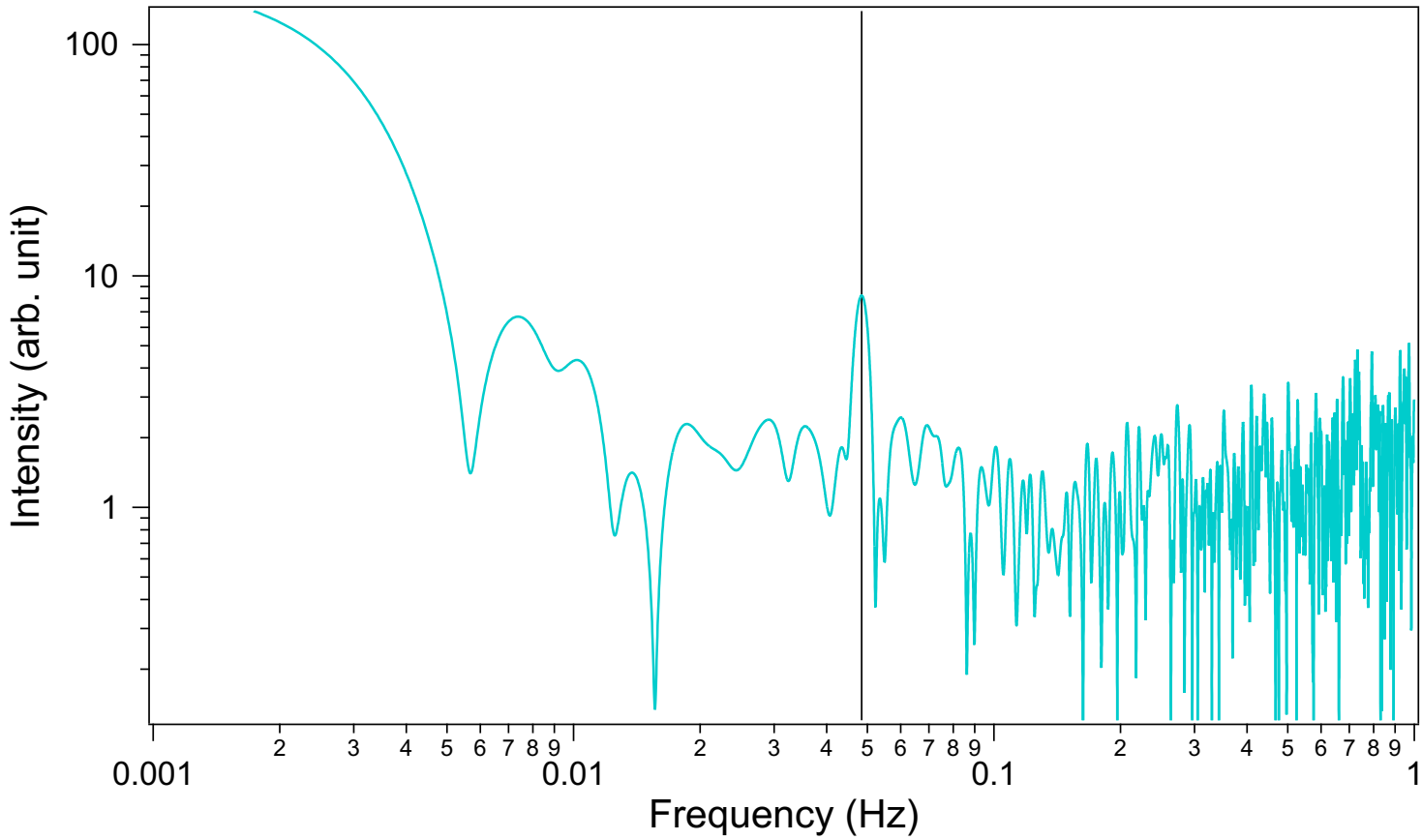

FIG. S4. FFT of SrO RHEED oscillation (shown in Fig. 4(f)) giving an average monolayer time of 20.64 ± 0.1 s.

The FFT of a SrO RHEED oscillation (Fig. 4(f)) is shown in Fig. S4. From it an average oscillation periodicity of 20.64 ± 0.1 s is derived. Note that hand counting gives similarly accurate results when sufficient oscillations are present. Given the RHEED oscillation period corresponds to the growth of the smallest charge neutral formula unit of SrO, which is half of the distance between the SrO (100) planes within the rock salt structure (d_{200}), [32] in one period a SrO film thickness of

$$d_{200} = \frac{5.161\times10^{-8}\text{cm}}{2} = 2.580\times10^{-8}\text{cm}$$

is grown. As it takes one period (20.6 s) to grow this thickness and the density of strontium atoms in SrO is 2.91×10^{22} atoms/cm^3, the strontium flux is

$$\text{Sr flux} = \frac{2.91\times10^{22}\ {}^{\text{atoms}}/_{\text{cm}^3}\times2.580\times10^{-8}\text{cm}}{20.64 \pm 0.1\ \text{s}} = (3.64 \pm 0.02)\times10^{13}\,\frac{\text{atoms}}{\text{cm}^2\text{s}}$$

Assuming that the $La_{0.5}Sr_{0.5}CoO_{3-\delta}$ film is commensurately strained to $LaAlO_3$ (100), for an in-plane lattice pseudo-cubic lattice parameter of 3.794 Å, the shutter time for 1/2 monolayer of SrO is calculated to be

$$\text{Sr shutter time} = {}^{1}/_{2}\times\frac{\frac{1}{(3.794\times10^{-8})^2}\,\frac{\text{atoms}}{\text{cm}^2}}{(3.64 \pm 0.02)\times10^{13}\,\frac{\text{atoms}}{\text{cm}^2\text{s}}} = 9.55 \pm 0.05\ \text{s}$$

Preparation recipes and atomic force microscopy images of prepared substrates

TABLE S2. Substrate preparation recipes and corresponding atomic force microscopy image

Substrate	Etching	Annealing	AFM image
Al_2O_3 (001)	None	1050 °C for 6 h in air Ref. [33]	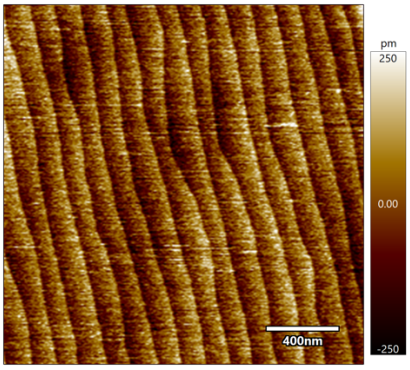
Al_2O_3 $(1\bar{1}2)$	None	1050 °C for 6 h in air	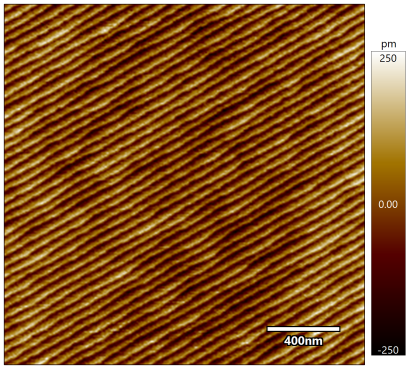
$SrTiO_3$ (100)	30 s in 7:1 buffered HF	950 °C for 1 h in O_2 Ref. [34]	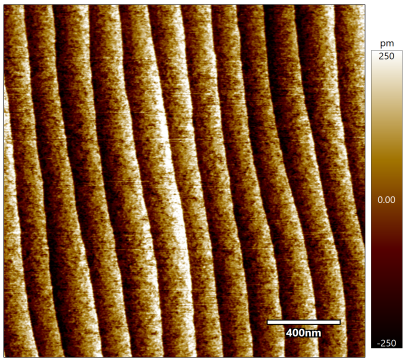
YSZ (111)	None	1150 °C for 3 h in air Ref. [35]	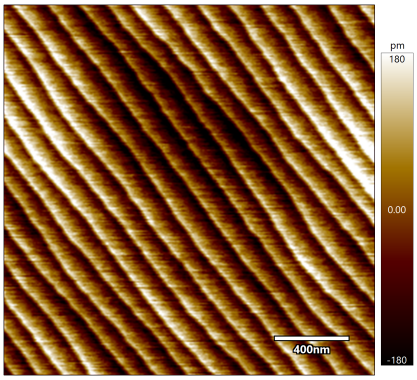

TiO_2 (110)	3 min in 10 vol% HCl followed by 10 min in 23 vol% HF	800 °C for 3 h in air Ref. [36]	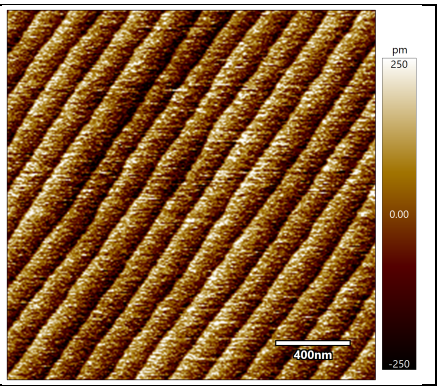

Binary oxide/metal thin film characterization

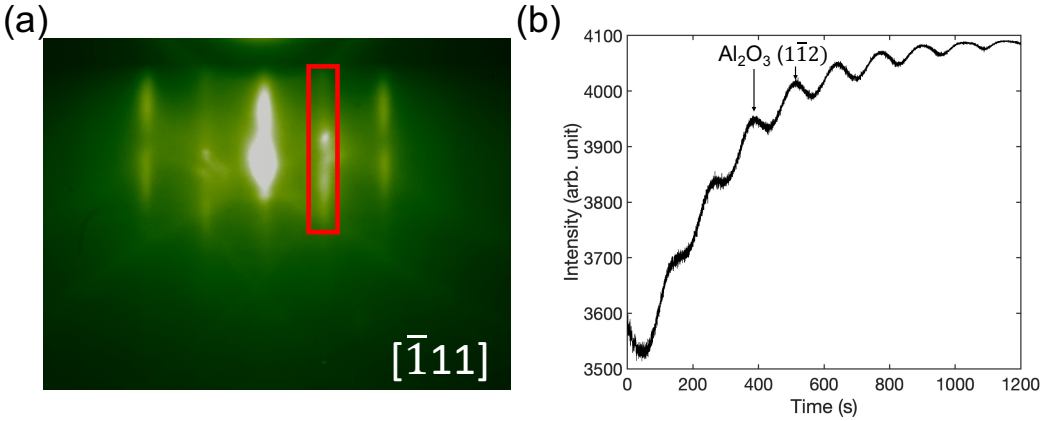

FIG. S5. Al_2O_3 /Al_2O_3 (1$\bar{1}$2). (a) RHEED pattern along the Al_2O_3 [$\bar{1}$11] direction, (b) RHEED oscillations recorded using the area outlined in red where each periodicity corresponds to the Al_2O_3 (1$\bar{1}$2) interplanar spacing.

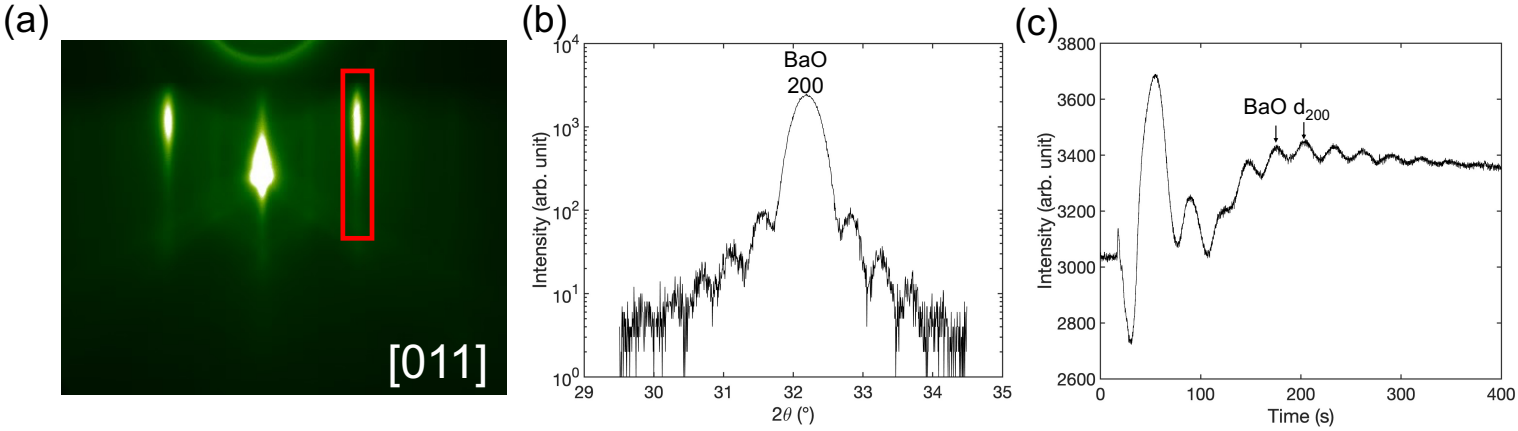

FIG. S6, BaO/$SrTiO_3$ (100). (a) RHEED pattern along the $SrTiO_3$ [011] direction, (b) XRD θ-2θ scan, and (c) RHEED oscillations recorded using the area outlined in red where each period of the oscillation corresponds to half of the distance between the (100) planes of BaO (d_{200}). For the *ex situ* XRR measurements, the film was capped with 3 nm of amorphous Al_2O_3.

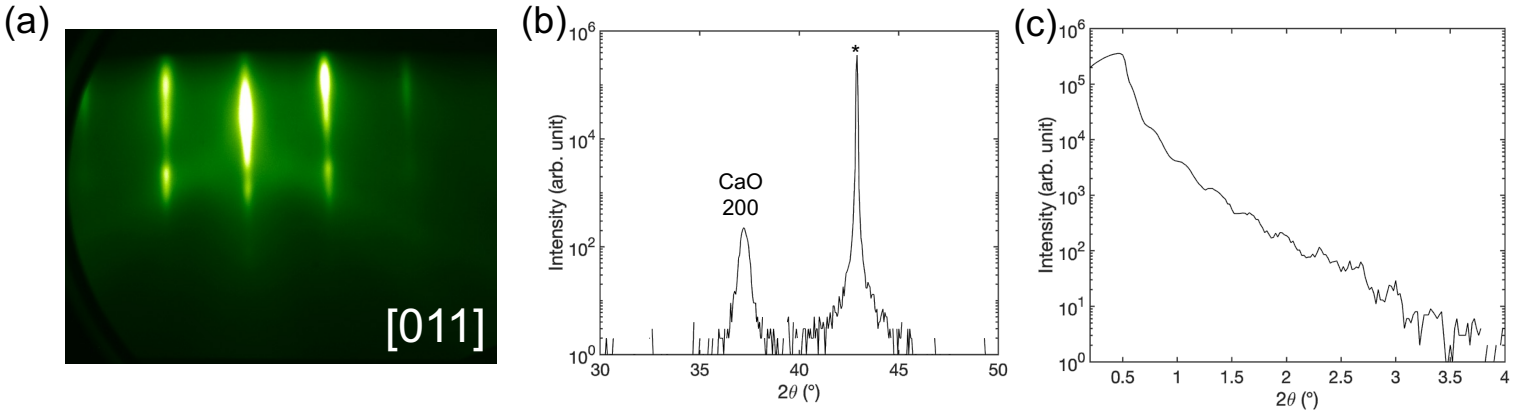

FIG. S7. CaO/MgO (100). (a) RHEED pattern along the MgO [011] direction, (b) XRD θ-2θ scan, and (c) X-ray reflectivity spectrum. The asterisk (*) indicates the substrate reflection. For the *ex situ* XRR measurements, the film was capped with 5 nm of amorphous NbO_2.

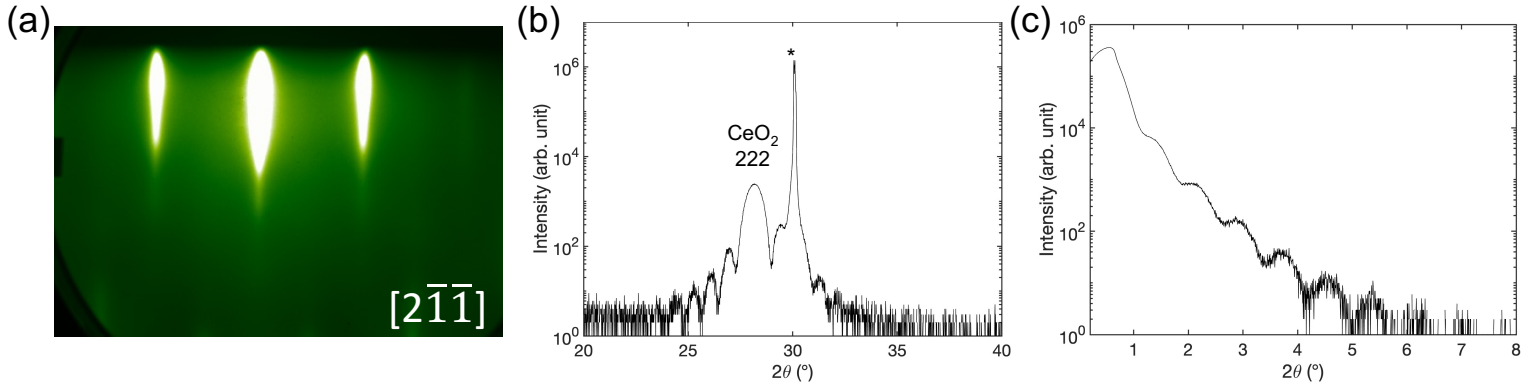

FIG. S8. CeO_2/YSZ (111). (a) RHEED pattern along the YSZ [$2\bar{1}\bar{1}$] direction, (b) XRD θ-2θ scan, and (c) X-ray reflectivity spectrum. The asterisk (*) indicates the substrate reflection.

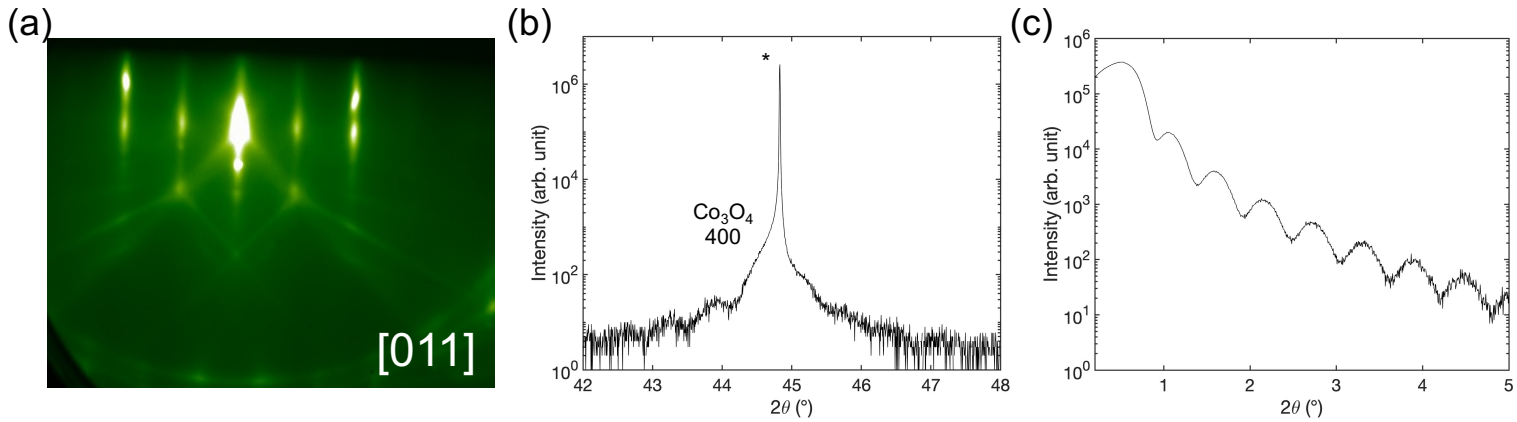

FIG. S9. Co_3O_4/$MgAl_2O_4$ (100). (a) RHEED pattern along the $MgAl_2O_4$ [011] direction, (b) XRD θ-2θ scan, and (c) X-ray reflectivity spectrum. The asterisk (*) indicates the substrate reflection.

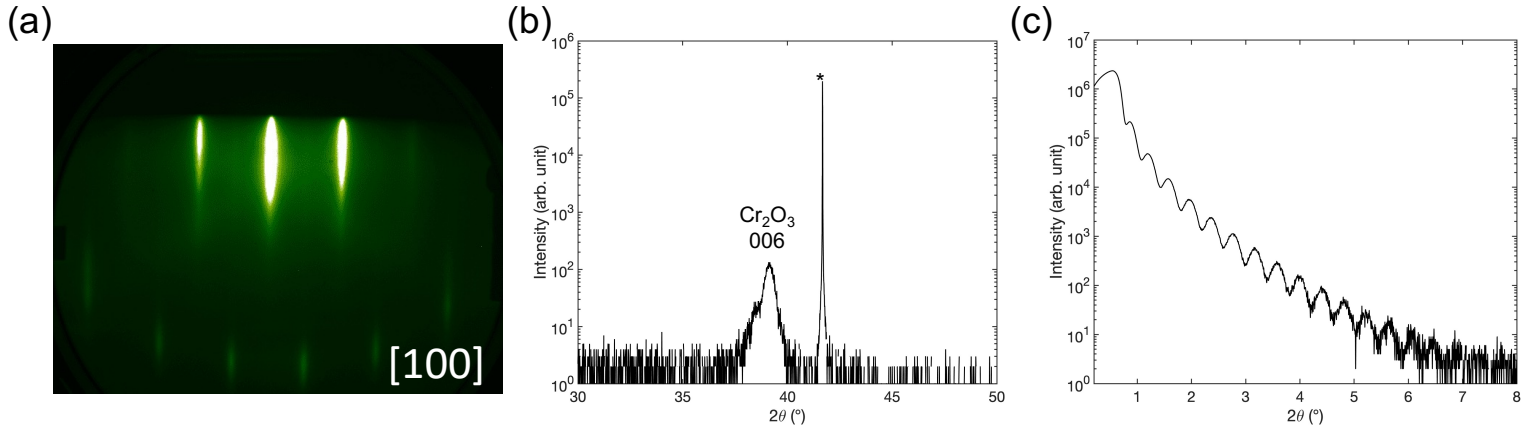

FIG. S10. Cr_2O_3/Al_2O_3 (001) (a) RHEED pattern along the Al_2O_3 [100] direction, (b) XRD θ-2θ scan, and (c) XRR spectrum. The asterisk (*) indicates the substrate reflection.

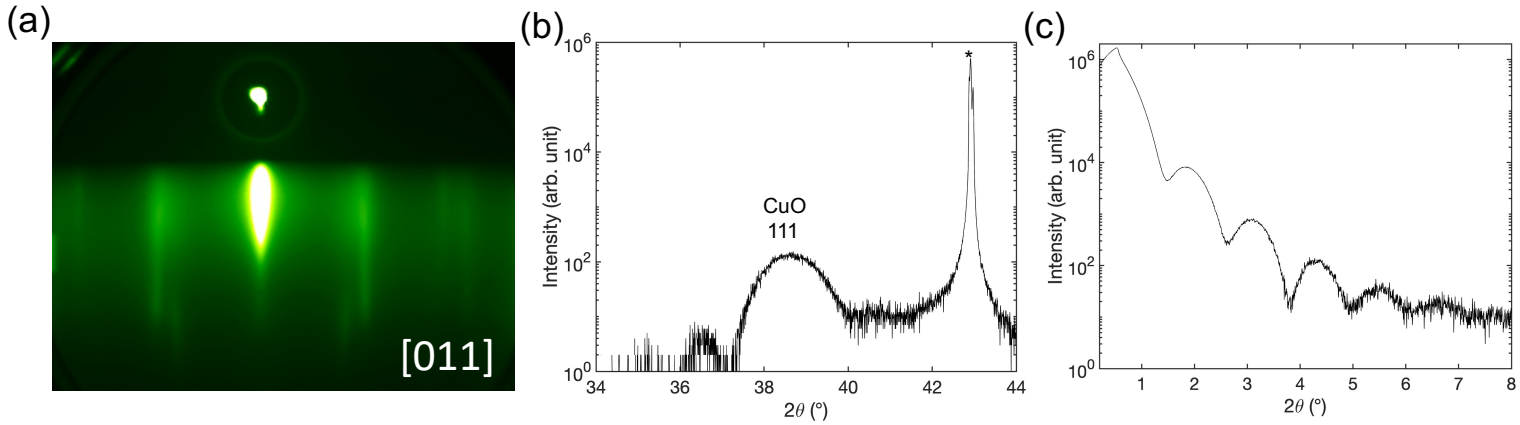

FIG. S11. CuO/MgO (100). (a) RHEED pattern along the MgO [011] direction, (b) XRD θ-2θ scan, and (c) X-ray reflectivity spectrum. The asterisk (*) indicates the substrate reflection.

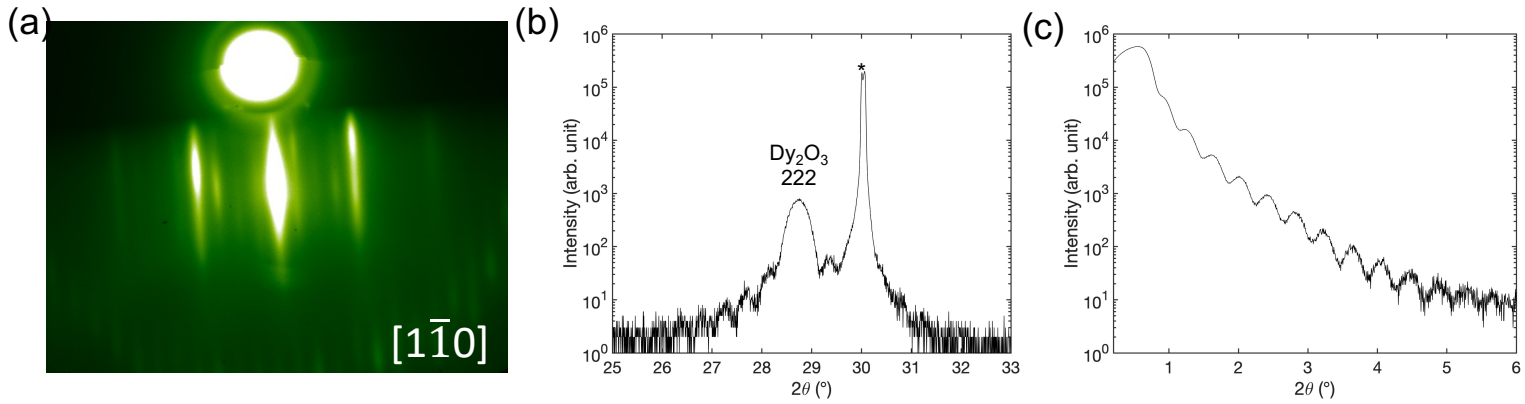

FIG. S12. Dy_2O_3/YSZ (111). (a) RHEED pattern along the YSZ [1$\bar{1}$0] direction, (b) XRD θ-2θ scan, and (c) X-ray reflectivity spectrum. The asterisk (*) indicates the substrate reflection.

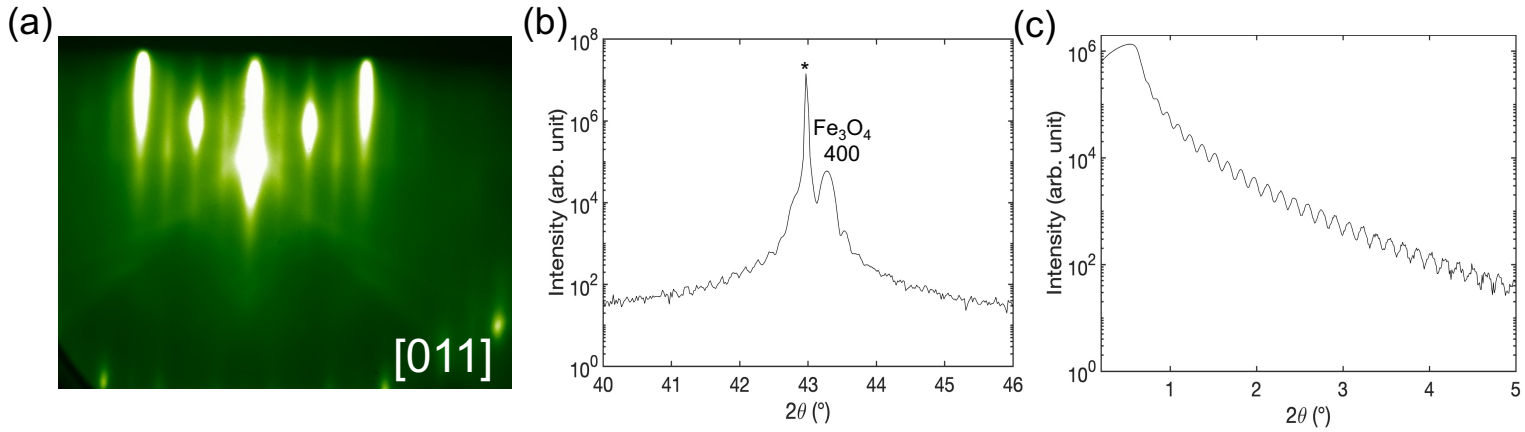

FIG. S13. Fe_3O_4/MgO (100). (a) RHEED pattern along the MgO [011] direction, (b) XRD θ-2θ scan, and (c) X-ray reflectivity spectrum. The asterisk (*) indicates the substrate reflection.

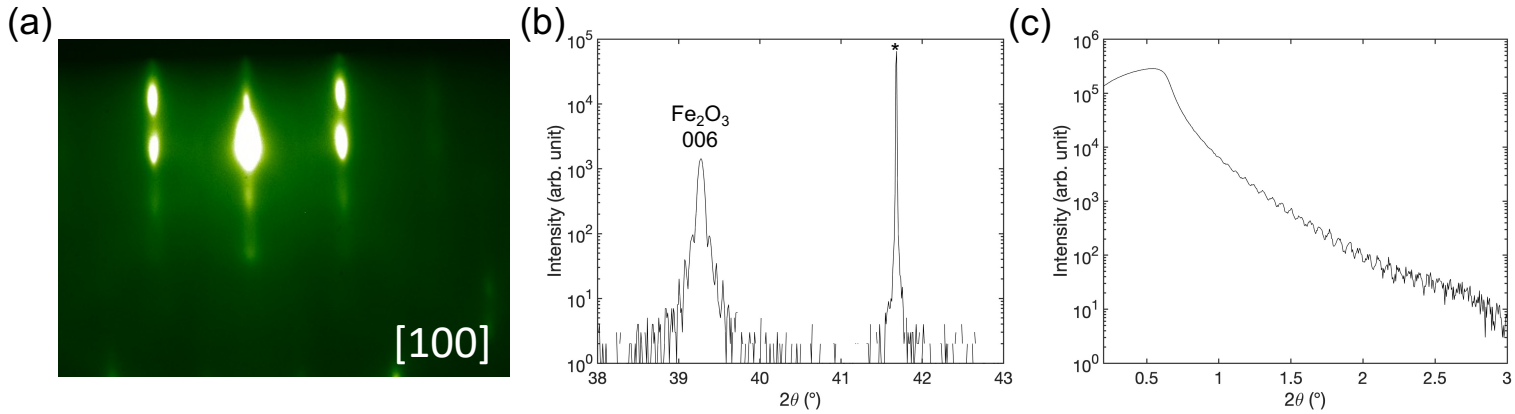

FIG. S14. Fe_2O_3/Al_2O_3 (001) (a) RHEED pattern along the Al_2O_3 [100] direction, (b) XRD θ-2θ scan, and (c) X-ray reflectivity spectrum. The asterisk (*) indicates the substrate reflection.

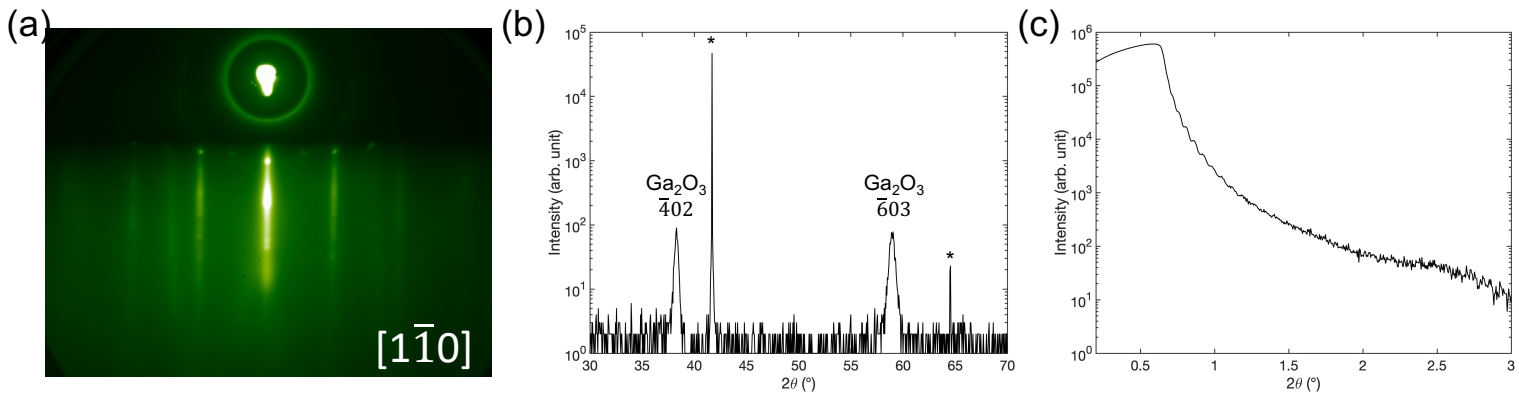

FIG. S15. β-Ga_2O_3/Al_2O_3 (001) (a) RHEED pattern along the Al_2O_3 [1$\bar{1}$0] direction, (b) XRD θ-2θ scan, and (c) X-ray reflectivity spectrum. The asterisk (*) indicates the substrate reflection.

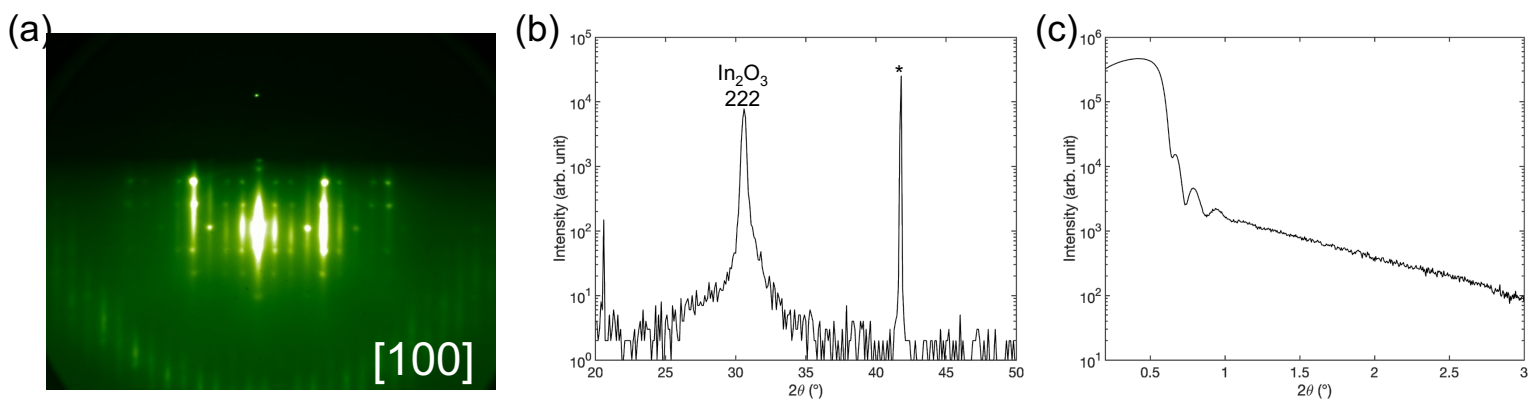

FIG. S16. In_2O_3/Al_2O_3 (001) (a) RHEED pattern along the Al_2O_3 [100] direction, (b) XRD θ-2θ scan, and (c) X-ray reflectivity spectrum. The asterisk (*) indicates the substrate reflection.

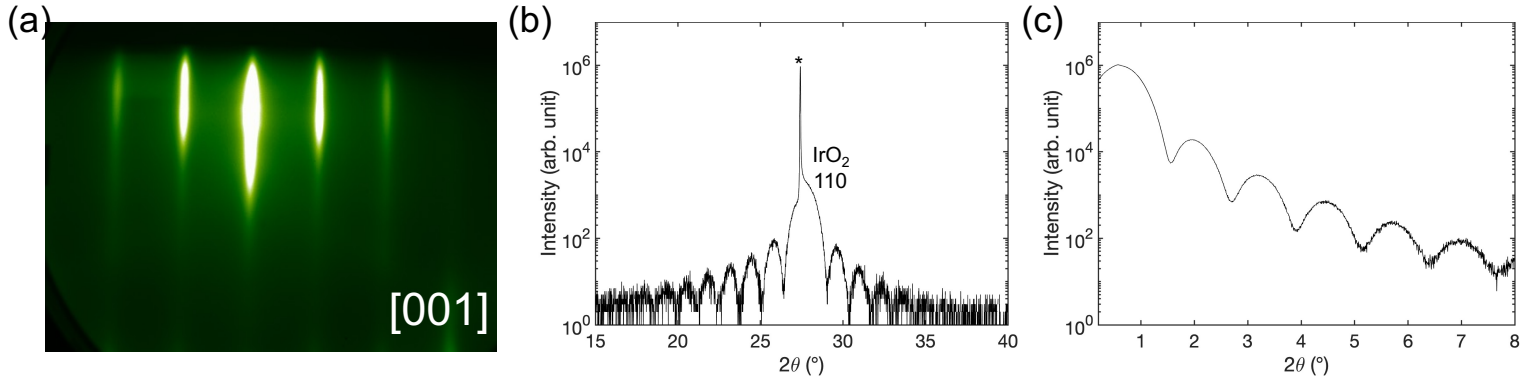

FIG. S17. IrO_2/TiO_2 (110). (a) RHEED pattern along the TiO_2 [001] direction, (b) XRD θ-2θ scan, and (c) X-ray reflectivity spectrum. The asterisk (*) indicates the substrate reflection.

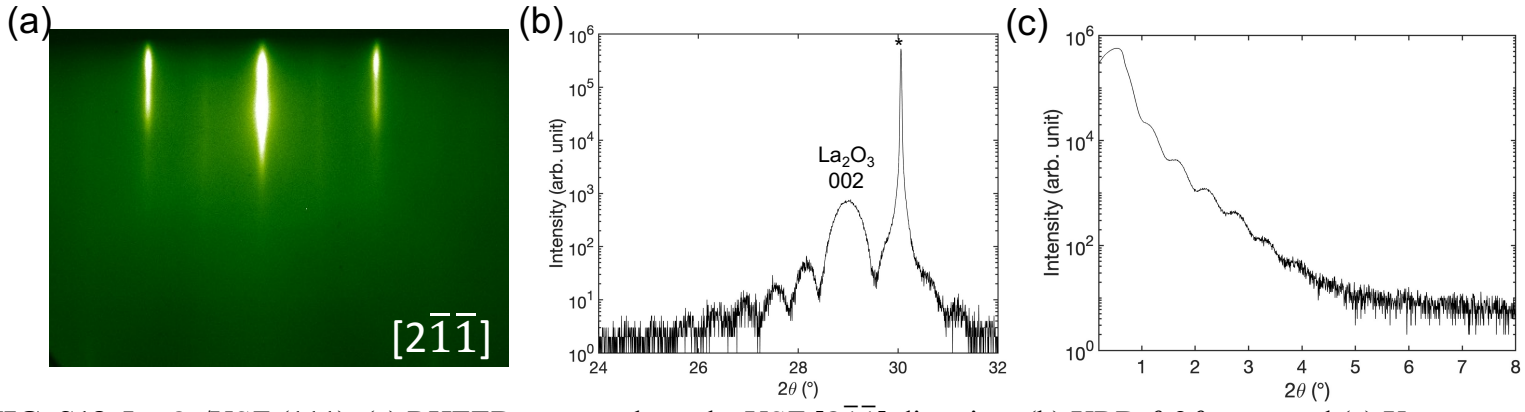

FIG. S18. La_2O_3/YSZ (111). (a) RHEED pattern along the YSZ [$2\bar{1}\bar{1}$] direction, (b) XRD θ-2θ scan, and (c) X-ray reflectivity spectrum. The asterisk (*) indicates the substrate reflection.

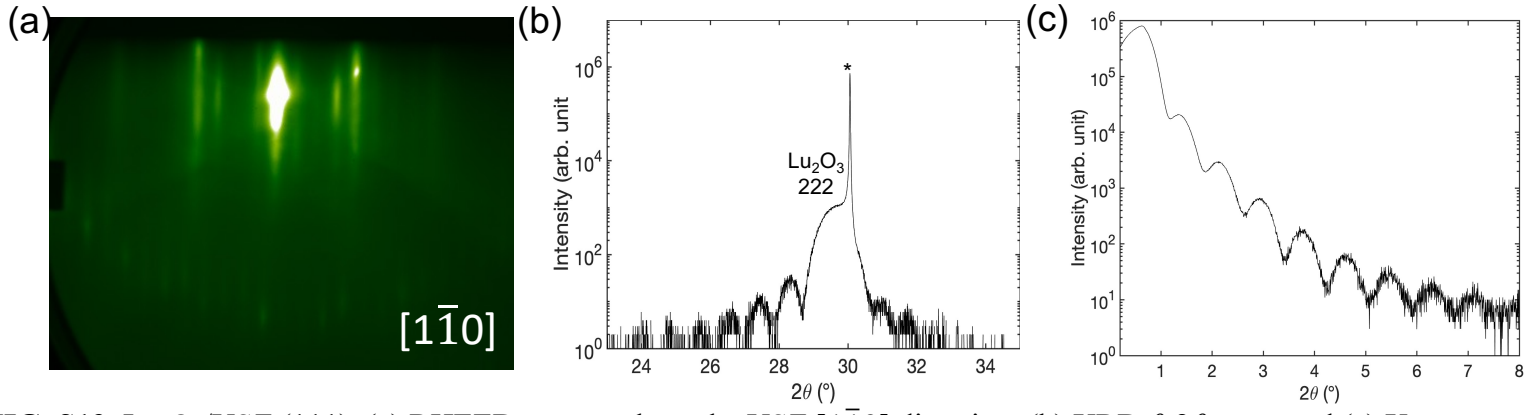

FIG. S19. Lu_2O_3/YSZ (111). (a) RHEED pattern along the YSZ [$1\bar{1}0$] direction, (b) XRD θ-2θ scan, and (c) X-ray reflectivity spectrum. The asterisk (*) indicates the substrate reflection.

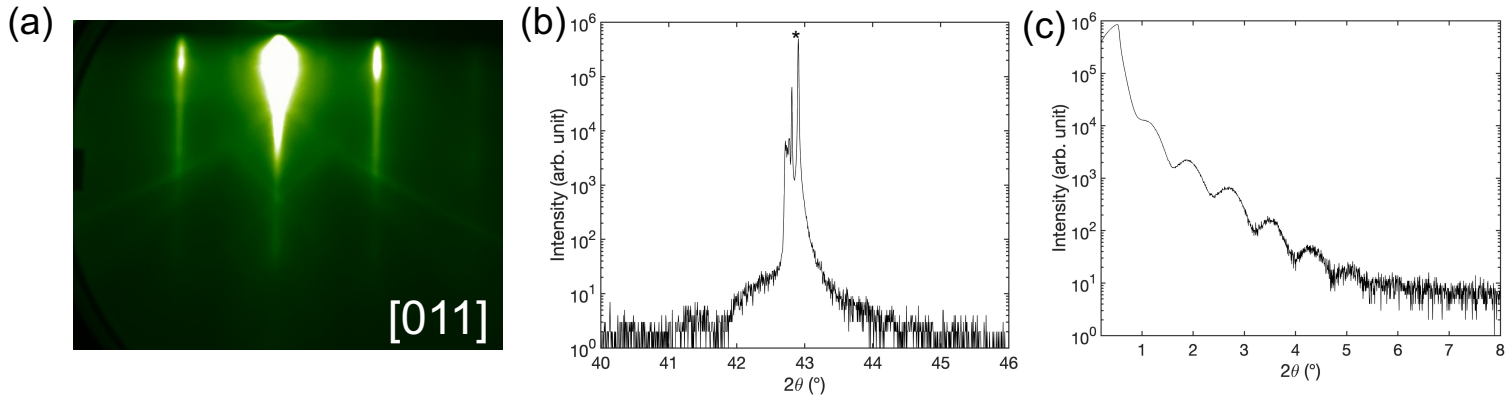

FIG. S20. MgO/1 nm Fe_3O_4/MgO (100). (a) RHEED pattern along the MgO [011] direction of the epitaxial MgO film, (b) XRD θ-2θ scan. The asterisk (*) indicates the substrate reflection. Note that the multiple peaks seen for the substrate 200 reflection arise due to the imperfect nature of MgO substrates (many subgrains), which are grown using arc melting. (c) X-ray reflectivity spectrum. The 1 nm Fe_3O_4 layer is used to create a well-defined interface for XRR, which is described in more detail in the section on MgO calibration below.

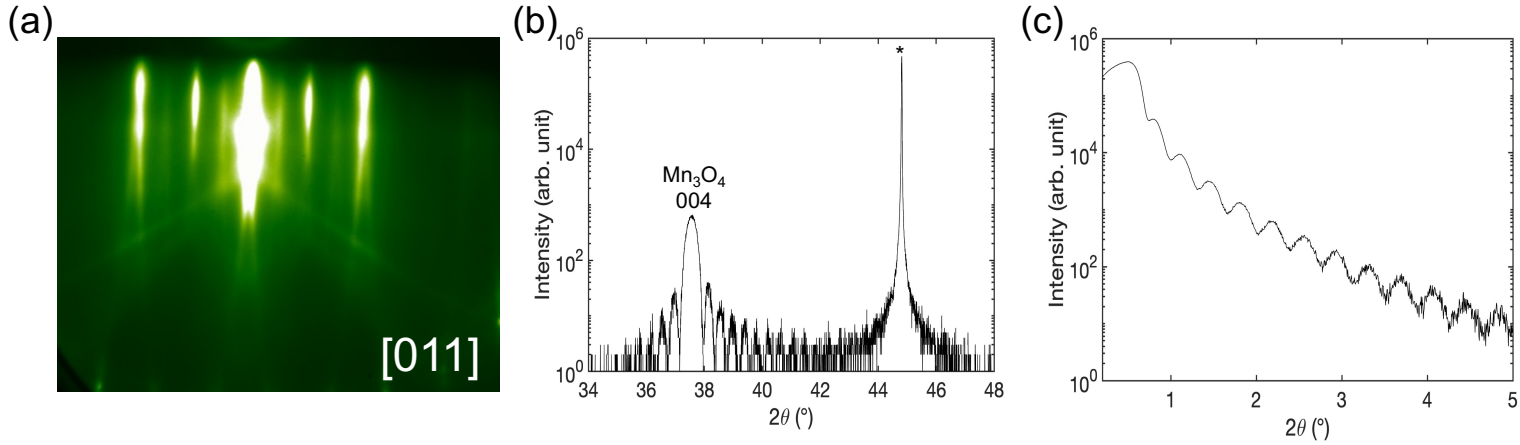

FIG. S21. Mn_3O_4/$MgAl_2O_4$ (100). (a) RHEED pattern along the $MgAl_2O_4$ [011] direction, (b) XRD θ-2θ scan, and (c) X-ray reflectivity spectrum. The asterisk (*) indicates the substrate reflection.

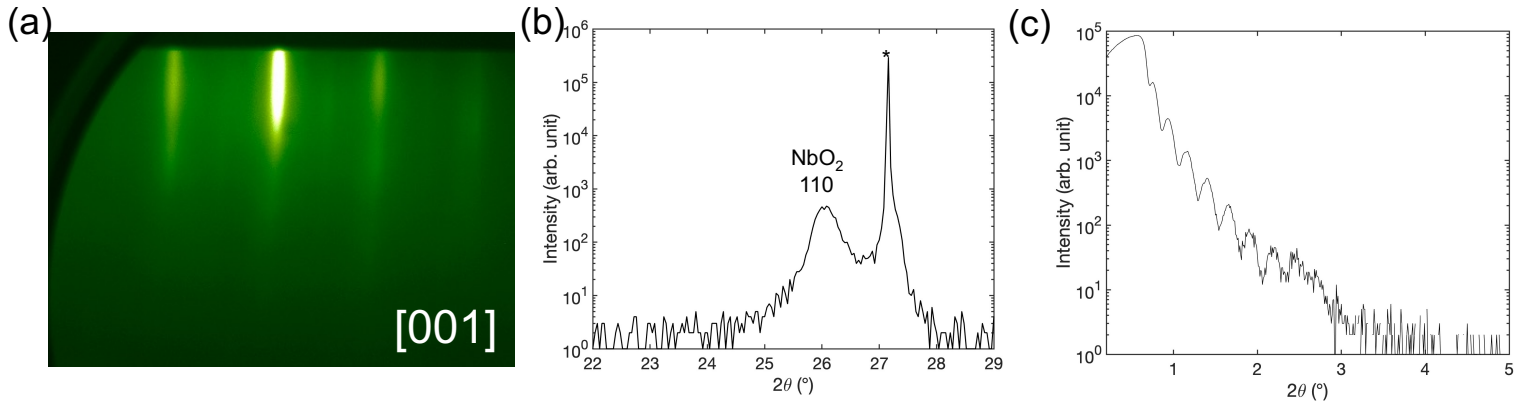

FIG. S22. NbO_2/MgF_2 (110). (a) RHEED pattern along the MgF_2 [001] direction, (b) XRD θ-2θ scan, and (c) X-ray reflectivity spectrum. The asterisk (*) indicates the substrate reflection.

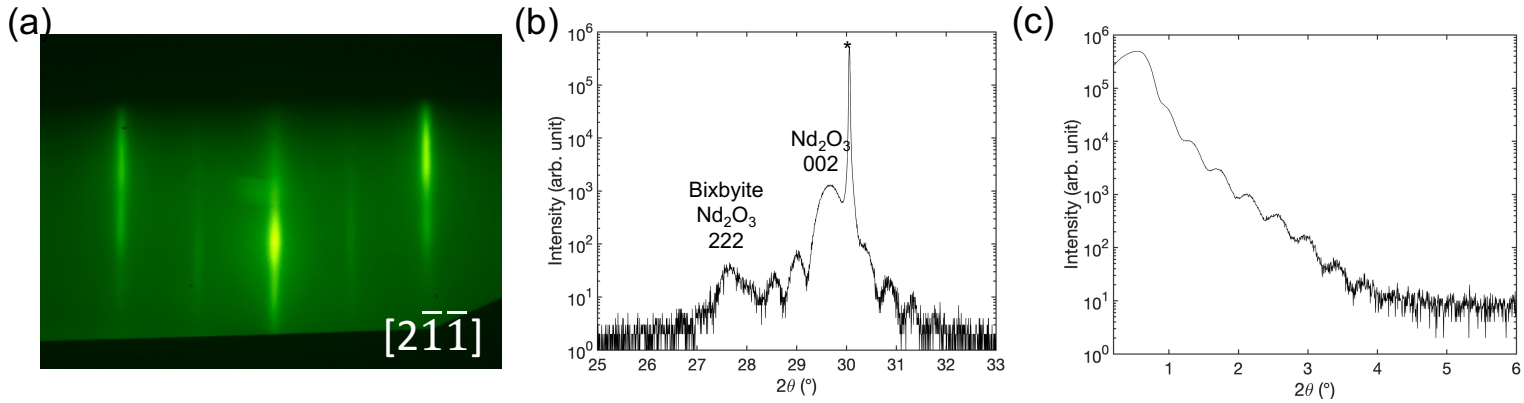

FIG. S23. Nd_2O_3/YSZ (111). (a) RHEED pattern along the YSZ [2$\bar{1}\bar{1}$] direction, (b) XRD θ-2θ scan, and (c) X-ray reflectivity spectrum. The asterisk (*) indicates the substrate reflection.

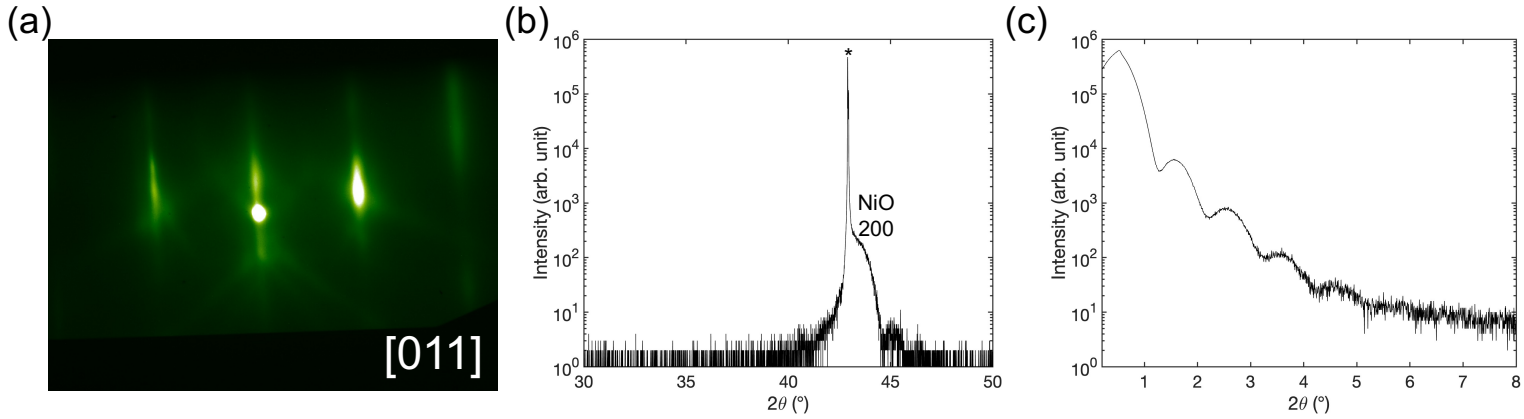

FIG. S24. NiO/MgO (100). (a) RHEED pattern along the MgO [011] direction, (b) XRD θ-2θ scan, and (c) X-ray reflectivity spectrum. The asterisk (*) indicates the substrate reflection.

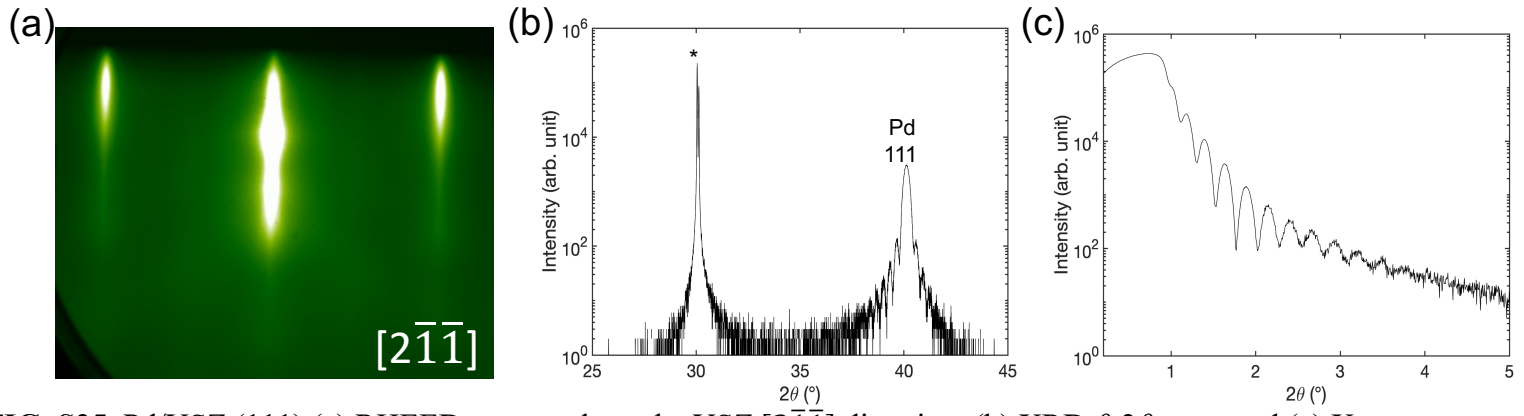

FIG. S25. Pd/YSZ (111) (a) RHEED pattern along the YSZ [2$\bar{1}\bar{1}$] direction, (b) XRD θ-2θ scan, and (c) X-ray reflectivity spectrum. The asterisk (*) indicates the substrate reflection.

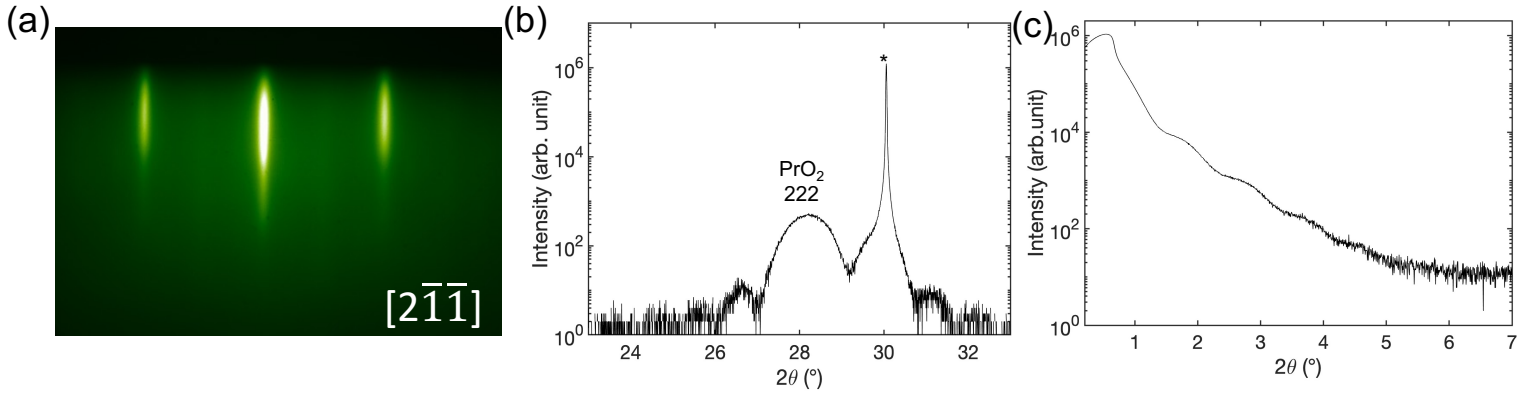

FIG. S26. PrO_2/YSZ (111). (a) RHEED pattern along the YSZ [2$\bar{1}\bar{1}$] direction, (b) XRD θ-2θ scan, and (c) X-ray reflectivity spectrum. The asterisk (*) indicates the substrate reflection.

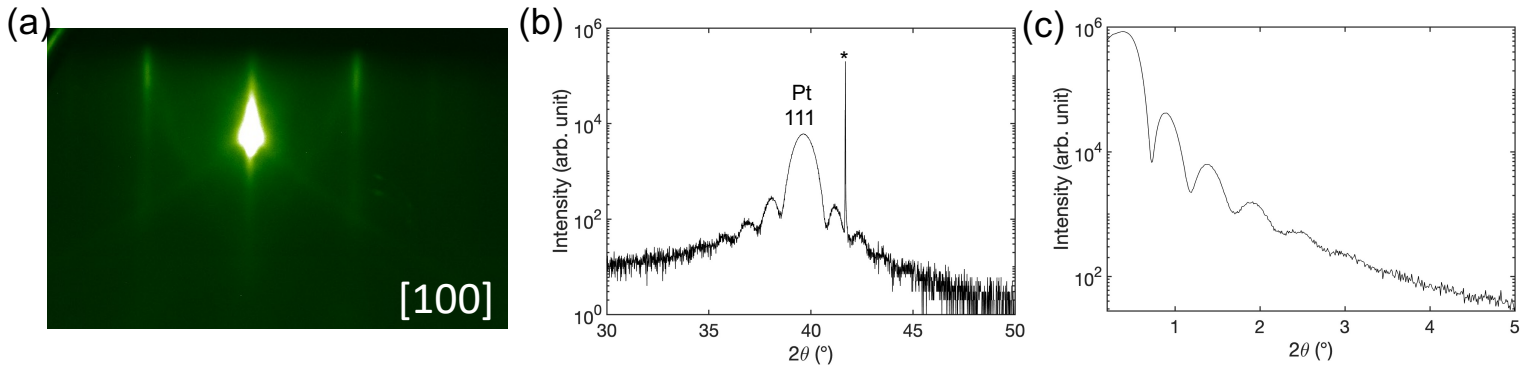

FIG. S27. Pt/Al_2O_3 (001) (a) RHEED pattern along the Al_2O_3 [100] direction, (b) XRD θ-2θ scan, and (c) X-ray reflectivity spectrum. The asterisk (*) indicates the substrate reflection.

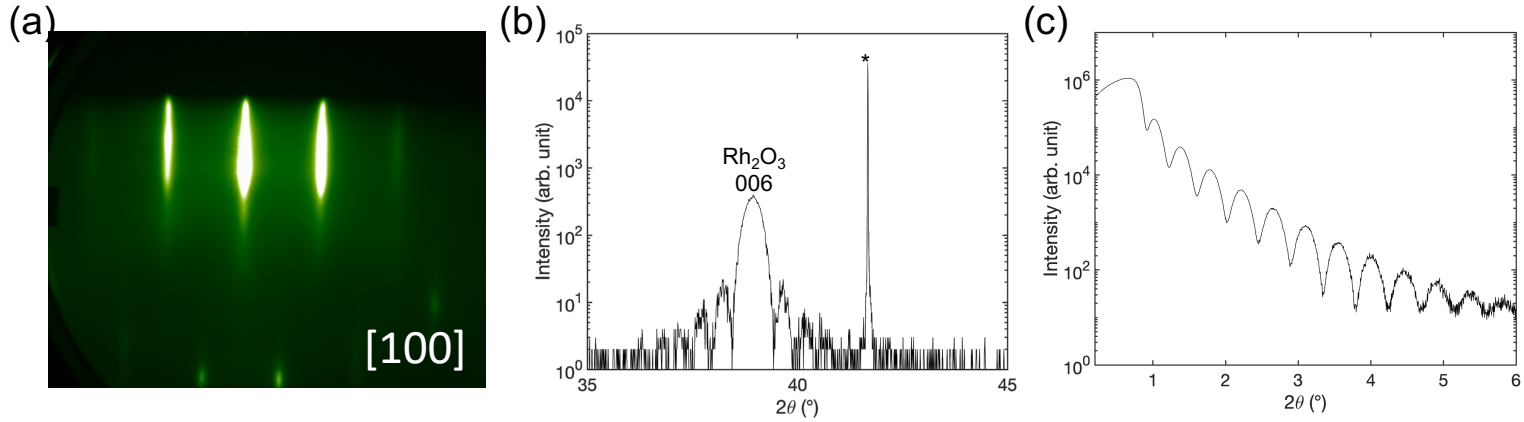

FIG. S28. Rh_2O_3/Al_2O_3 (001) (a) RHEED pattern along the Al_2O_3 [100] direction, (b) XRD θ-2θ scan, and (c) X-ray reflectivity spectrum. The asterisk (*) indicates the substrate reflection.

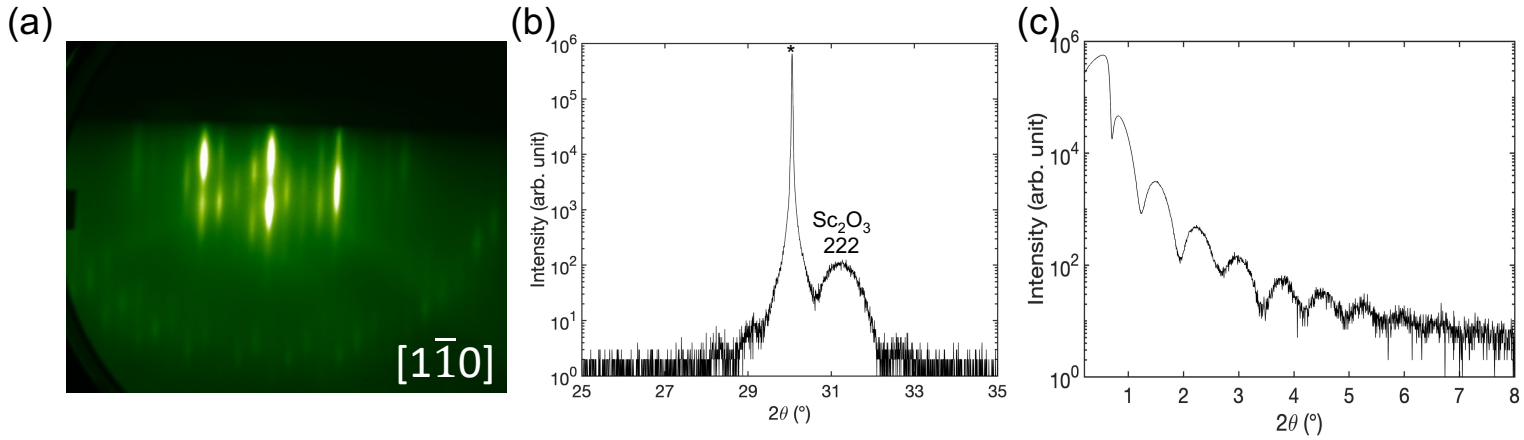

FIG. S29. Sc_2O_3/YSZ (111). (a) RHEED pattern along the YSZ [1$\bar{1}$0] direction, (b) XRD θ-2θ scan, and (c) X-ray reflectivity spectrum. The asterisk (*) indicates the substrate reflection.

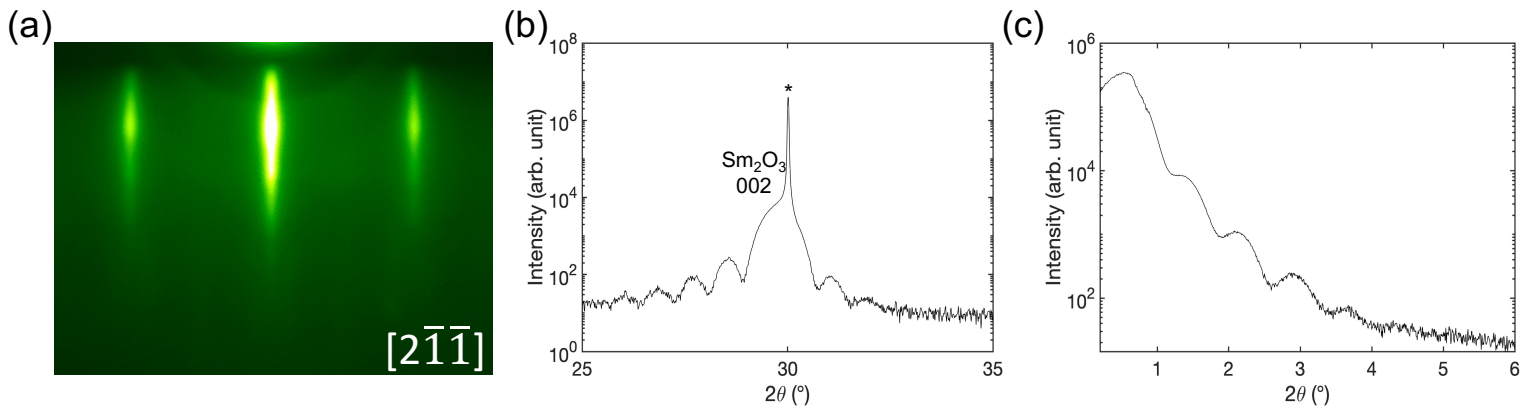

FIG. S30. Sm_2O_3/YSZ (111). (a) RHEED pattern along the YSZ [2$\bar{1}\bar{1}$] direction, (b) XRD θ-2θ scan, and (c) X-ray reflectivity spectrum. The asterisk (*) indicates the substrate reflection.

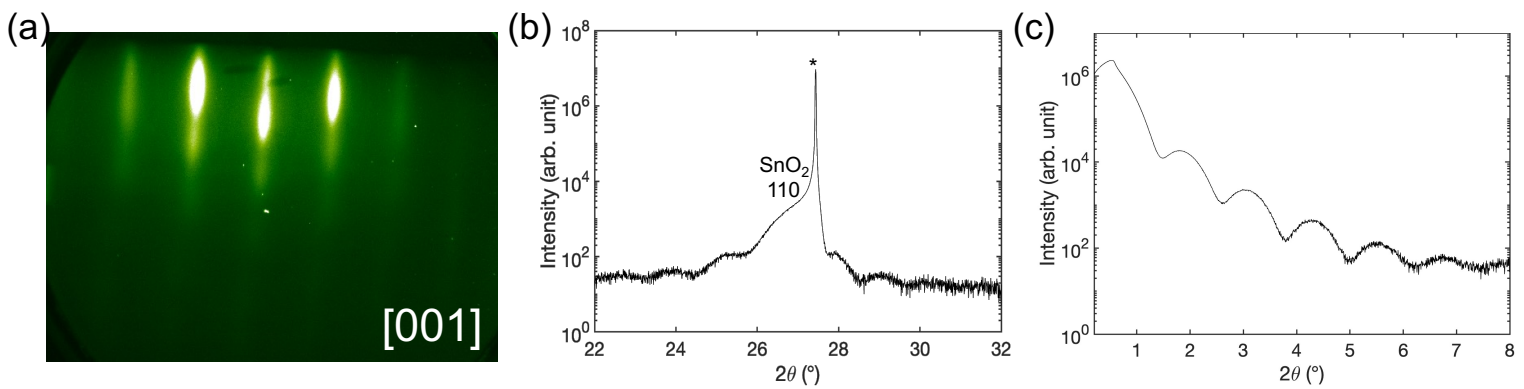

FIG. S31. SnO_2/TiO_2 (110). (a) RHEED pattern along the TiO_2 [001] direction, (b) XRD θ-2θ scan, and (c) X-ray reflectivity spectrum. The asterisk (*) indicates the substrate reflection.

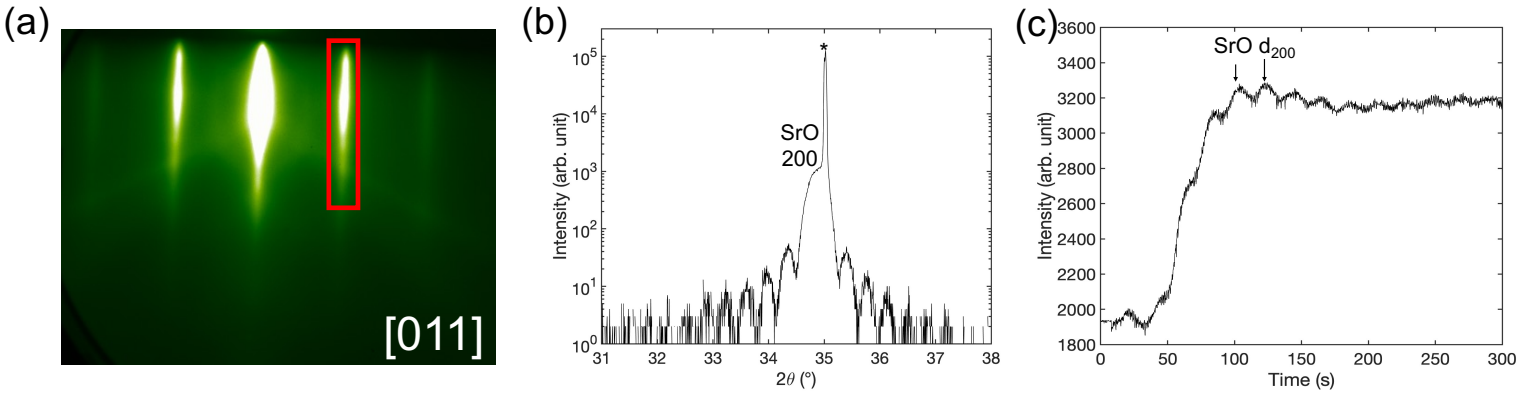

FIG. S32. SrO/YSZ (100). (a) RHEED pattern along the YSZ [011] direction, (b) XRD θ-2θ, and (c) RHEED oscillations recorded using the area outlined in red where each period of the oscillation corresponds to half of the distance between the (100) planes of SrO (d_{200}). The asterisk (*) indicates the substrate reflection. For the *ex situ* XRR measurements, the film was capped with 10 nm of amorphous TiO_2.

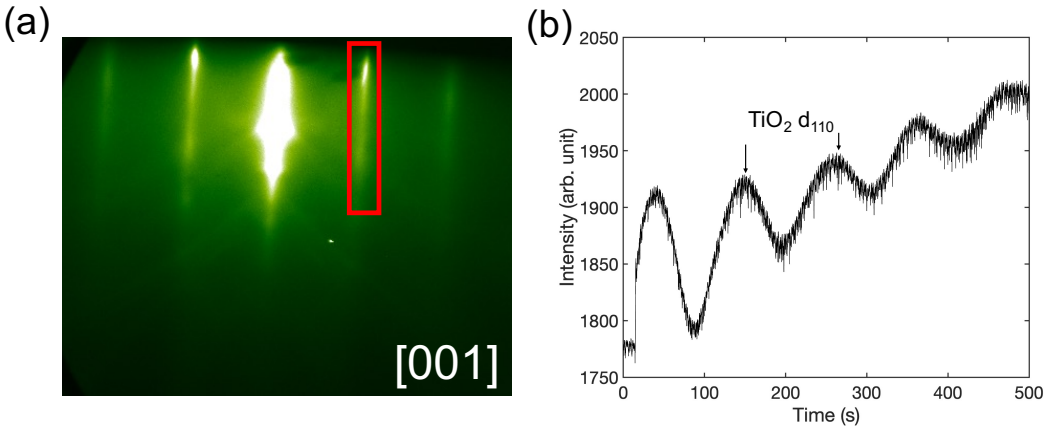

FIG. S33. TiO_2/TiO_2 (110). (a) RHEED pattern along the TiO_2 [001] direction, (b) RHEED oscillations recorded using the area outlined in red where each period of the oscillation corresponds to the TiO_2 (110) interplanar spacing.

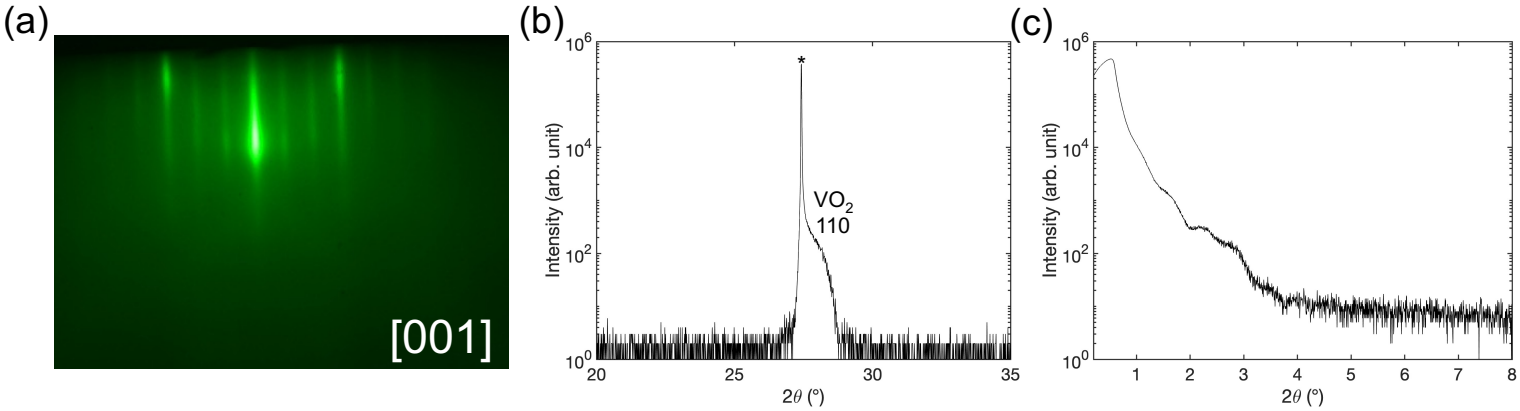

FIG. S34. VO_2/TiO_2 (110). (a) RHEED pattern along the TiO_2 [001] direction, (b) XRD θ-2θ scan, and (c) XRR spectrum. The asterisk (*) indicates the substrate reflection.

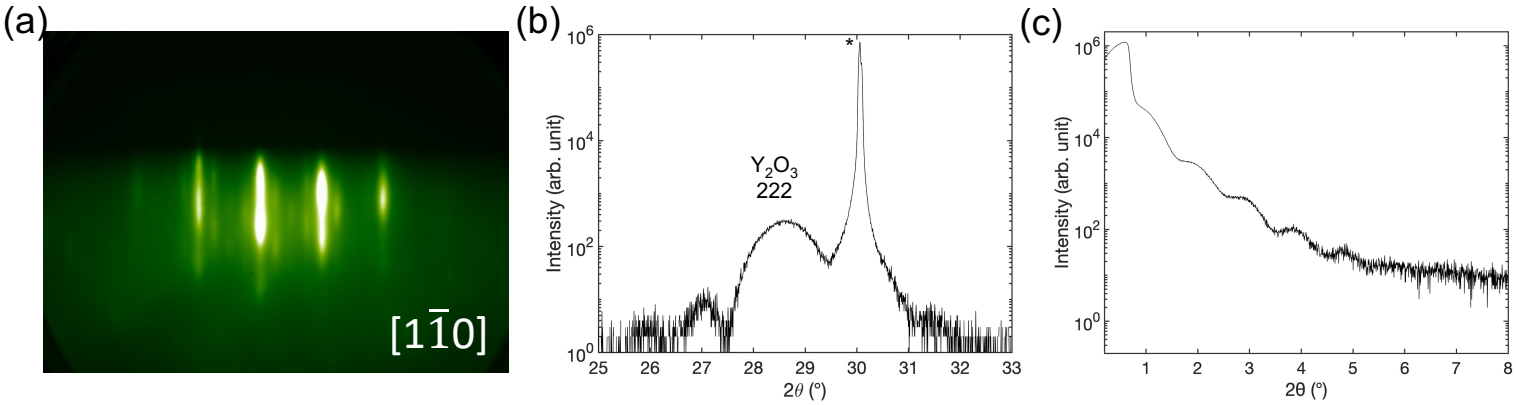

FIG. S35. Y_2O_3/YSZ (111). (a) RHEED pattern along the YSZ [1$\bar{1}$0] direction, (b) XRD θ-2θ scan, and (c) X-ray reflectivity spectrum. The asterisk (*) indicates the substrate reflection.

MgO calibration

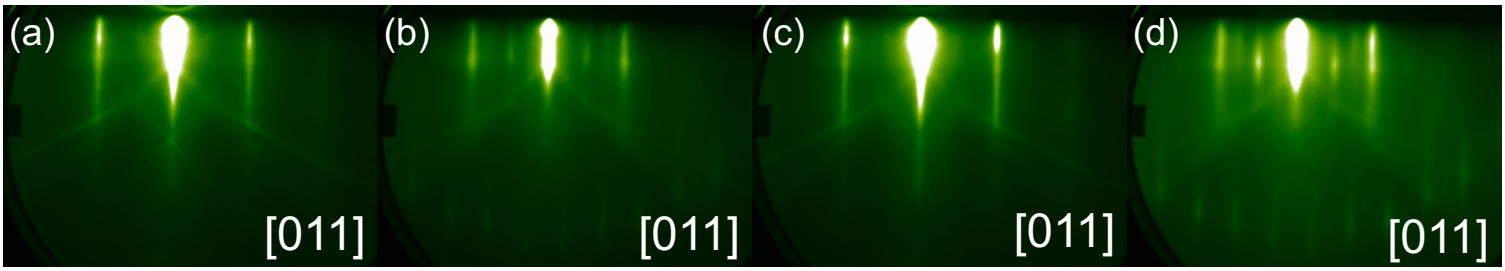

FIG. S36. Evolution of 1 nm Fe_3O_4/11 nm MgO/1 nm Fe_3O_4/MgO (100) trilayer growth viewed along the [011] azimuth where (a), (b), (c), and (d) correspond to the bare substrate, 1 nm of Fe_3O_4, 11 nm MgO/1 nm Fe_3O_4, and 1 nm Fe_3O_4/11 nm MgO/1 nm Fe_3O_4, respectively.

Due to the high surface mobility of MgO adatoms, [37] RHEED oscillations (which arise from growth in an atom layer by atom layer growth mode) are only expected at very low temperatures (<100 K) in MgO homoepitaxial growth; [38] by 450 °C the growth mode is island growth and transitions to step-flow at temperatures above 650 °C. [39] The absence of RHEED oscillations at room temperature is also observed in homoepitaxial growths of related systems such as NaCl, where again the NaCl adatoms have high surface mobility. [40] In this case one needs to use XRR to establish the magnesium flux. A well-defined interface needs to be created, however, such that the epitaxial MgO can be differentiated from the substrate with the same electron density. There are a few binary oxides that are lattice matched to MgO that can be used as ultra-thin interface layers, such as CoO, NiO, and Fe_3O_4. In the example given here, we chose to use 1 nm of Fe_3O_4 as both the interface layer and capping layer. The RHEED patterns during the Fe_3O_4/MgO/Fe_3O_4 growth are outlined in Fig. S36 above where the characteristics features of spinel and rock salt structures are well differentiated. The abrupt interface between Fe_3O_4 and MgO is also evidenced by the well-defined XRR spectrum shown in Fig. S20 above.

Nd_2O_3 calibration

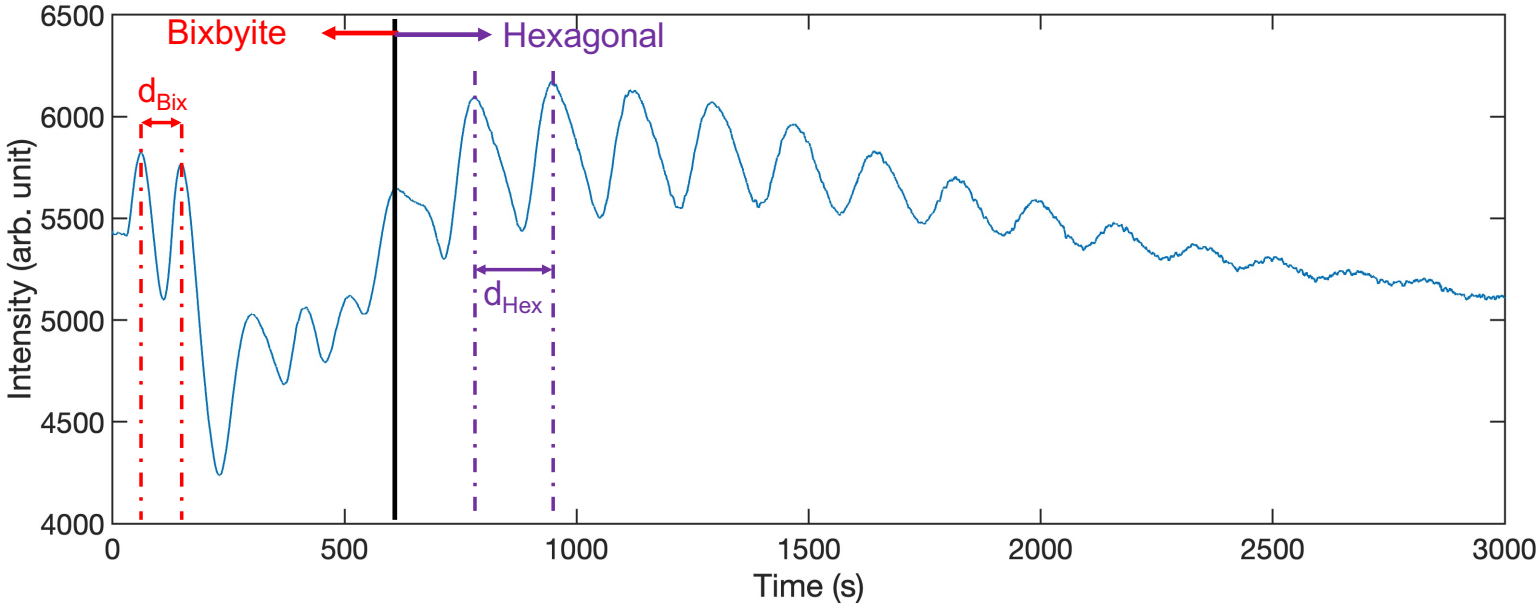

FIG. S37. Evolution of the RHEED oscillation profile during the growth of Nd_2O_3/YSZ (111). The difference in oscillation periodicities is attributed to differences in the lattice parameters of the bixbyite and hexagonal polymorphs of Nd_2O_3, where a transition from the bixbyite polymorph to the hexagonal polymorph occurs.

For rare-earth sesquioxides, there are a few competing structural polymorphs including cubic bixbyite and hexagonal phases. In bulk, the bixbyite structure is the most stable polymorph for the later rare-earths from europium to lutetium, but for the early rare-earths lanthanum, neodymium and samarium, the hexagonal polymorph is more stable. [41] As the energies between the competing polymorphs are close at the cross-over, epitaxial stabilization can play an important role in which polymorph appears in thin films. [42–47] For example, when deposited onto YSZ(111) one

often forms a mixture of bixbyite and hexagonal phases even though hexagonal phases are thermodynamically more stable in the absence of a substrate. For accurate flux calculation, one needs to identify a growth window that consistently yields single-phase films as the mass density between the two polymorphs can be larger than 10%. For La_2O_3 and Sm_2O_3 we have identified growth conditions that yield single-phase hexagonal structures, but for Nd_2O_3 our optimized growth condition still yields up to 3 monolayers of the bixbyite phase before the structure transforms into a hexagonal phase. The differences in the lattice parameters between the initial bixbyite growth and subsequent hexagonal growth are readily differentiated based on the periodicity of the RHEED oscillations, as shown in Fig. S37. We are confident that the bixbyite phase only exists in the interface regions because (1) the bixbyite peak intensity in XRD is constant regardless of the total film thickness, (2) there is no sign of a lateral mixture (superposition) of the two phases in RHEED, and (3) the transition from the interfacial cubic phase to bulk-stable hexagonal phase is also observed in La_2O_3 grown on silicon. [48]

The accuracy of the flux inferred from the growth of a calibration film of Nd_2O_3 thus depends on selective analysis of only the hexagonal layer. This can be done by (1) growth of a thick hexagonal layer (> 35 nm) such that the XRR thickness mostly derives from the hexagonal layer and more accurately (2) FFT of RHEED oscillations occurring during the growth of only the hexagonal layers.

References

[1] C. M. Brooks, L. F. Kourkoutis, T. Heeg, J. Schubert, D. A. Muller, and D. G. Schlom, Appl. Phys. Lett. **94**, 162905 (2009).
[2] T. Maeda, M. Yoshimoto, T. Ohnishi, G. H. Lee, and H. Koinuma, J. Cryst. Growth **177**, 95 (1997).
[3] P. W. Palmberg, T. N. Rhodin, and C. J. Todd, Appl. Phys. Lett. **11**, 33 (1967).
[4] T. Ohnishi, M. Yoshimoto, G. H. Lee, T. Maeda, and H. Koinuma, J. Vac. Sci. Technol., A **15**, 2469 (1997).
[5] H. D. Li, X. N. Zhang, Z. Zhang, Z. X. Mei, X. L. Du, and Q. K. Xue, J. Appl. Phys. **102**, 046103 (2007).
[6] T. C. Kaspar, S. E. Chamberlin, M. E. Bowden, R. Colby, V. Shutthanandan, S. Manandhar, Y. Wang, P. V. Sushko, and S. A. Chambers, J. Phys.: Condens. Matter **26**, 135005 (2014).
[7] P. V. B. Pinho, A. Chartier, F. Miserque, D. Menut, and J.-B. Moussy, Mater. Res. Lett. **9**, 163 (2021).
[8] K. Kawaguchi, R. Kita, M. Nishiyama, and T. Morishita, J. Cryst. Growth **143**, 221 (1994).
[9] R. Dargis, D. Williams, R. Smith, E. Arkun, R. Roucka, A. Clark, and M. Lebby, ECS J. Solid State Sci. Technol. **1**, N24 (2012).
[10] P. Somers, A. Stesmans, V. V. Afanas'ev, W. Tian, L. F. Edge, and D. G. Schlom, J. Appl. Phys. **107**, 094502 (2010).
[11] G. Chern and Y. R. Chean, Jpn. J. Appl. Phys. **36**, 2813 (1997).
[12] A. Serrano, J. Rubio-Zuazo, J. López-Sánchez, I. Arnay, E. Salas-Colera, and G. R. Castro, J. Phys. Chem. C **122**, 16042 (2018).
[13] B. Feng, Z. Li, F. Cheng, L. Xu, T. Liu, Z. Huang, F. Li, J. Feng, X. Chen, Y. Wu, G. He, and S. Ding, Phys. Status Solidi **218**, 2000457 (2021).
[14] Z. Cheng, M. Hanke, P. Vogt, O. Bierwagen, and A. Trampert, Appl. Phys. Lett. **111**, 162104 (2017).
[15] K. H. L. Zhang, V. K. Lazarov, P. L. Galindo, F. E. Oropeza, D. J. Payne, H. H.-C. Lai, and R. G. Egdell, Cryst. Growth Des. **12**, 1000 (2012).
[16] O. Bierwagen and J. S. Speck, J. Appl. Phys. **107**, 113519 (2010).
[17] J. N. Nelson, J. P. Ruf, Y. Lee, C. Zeledon, J. K. Kawasaki, S. Moser, C. Jozwiak, E. Rotenberg, A. Bostwick, D. G. Schlom, K. M. Shen, and L. Moreschini, Phys. Rev. Mater. **3**, 064205 (2019).
[18] D. Reisinger, B. Blass, J. Klein, J. B. Philipp, M. Schonecke, A. Erb, L. Alff, and R. Gross, Appl. Phys. A **77**, 619 (2003).
[19] L. Ren, S. Wu, M. Yang, W. Zhou, and S. Li, J. Appl. Phys. **114**, 053907 (2013).
[20] Y. Du, G. Li, E. W. Peterson, J. Zhou, X. Zhang, R. Mu, Z. Dohnálek, M. Bowden, I. Lyubinetsky, and S. A. Chambers, Nanoscale **8**, 3119 (2016).
[21] K. M. Adkison, S.-L. Shang, B. J. Bocklund, D. Klimm, D. G. Schlom, and Z.-K. Liu, APL Mater. **8**, 081110 (2020).
[22] J. P. Ruf, H. Paik, N. J. Schreiber, H. P. Nair, L. Miao, J. K. Kawasaki, J. N. Nelson, B. D. Faeth, Y. Lee, B. H. Goodge, B. Pamuk, C. J. Fennie, L. F. Kourkoutis, D. G. Schlom, and K. M. Shen, Nat. Commun. **12**, 59 (2021).
[23] M. Y. Tsai, M. E. White, and J. S. Speck, J. Appl. Phys. **106**, 024911 (2009).
[24] J. K. Kawasaki, D. Baek, H. Paik, H. P. Nair, L. F. Kourkoutis, D. G. Schlom, and K. M. Shen, Phys. Rev. Mater. **2**, 054206 (2018).
[25] J. Jeong, N. B. Aetukuri, D. Passarello, S. D. Conradson, M. G. Samant, and S. S. P. Parkin, Proc. Natl. Acad. Sci. U. S. A. **112**, 1013 (2015).
[26] S. Yun, C.-S. Woo, G.-Y. Kim, P. Sharma, J. H. Lee, K. Chu, J. H. Song, S.-Y. Chung, J. Seidel, S.-Y. Choi, and C.-H. Yang, Appl. Phys. Lett. **107**, 252904 (2015).
[27] H. Mito, R. Nakamura, K. Koike, S. Sasa, M. Yano, S. Kobayashi, and K. Inaba, in *2018 IEEE International Meeting for Future of Electron Devices, Kansai (IMFEDK)* (IEEE, 2018), pp. 1–2.
[28] Y. Du, M. Gu, T. Varga, C. Wang, M. E. Bowden, and S. A. Chambers, ACS Appl. Mater. Interfaces **6**, 14253 (2014).
[29] M. Yano, K. Koike, M. Matsuo, T. Murayama, Y. Harada, and K. Inaba, Appl. Surf. Sci. **381**, 32 (2016).
[30] T. Makino, T. Asai, T. Takeuchi, K. Kaminaga, D. Oka, and T. Fukumura, Jpn. J. Appl. Phys. **59**, SCCB13 (2020).
[31] Y. Chen, D. M. Bagnall, H. Koh, K. Park, K. Hiraga, Z. Zhu, and T. Yao, J. Appl. Phys. **84**, 3912 (1998).
[32] T. Terashima, Y. Bando, K. Iijima, K. Yamamoto, K. Hirata, K. Hayashi, K. Kamigaki, and H. Terauchi, Phys.

Rev. Lett. **65**, 2684 (1990).
[33] R. Jinno, T. Uchida, K. Kaneko, and S. Fujita, Appl. Phys. Express **9**, 071101 (2016).
[34] G. Koster, B. L. Kropman, G. J. H. M. Rijnders, D. H. A. Blank, and H. Rogalla, Appl. Phys. Lett. **73**, 2920 (1998).
[35] H. Ohta, M. Orita, M. Hirano, and H. Hosono, J. Appl. Phys. **91**, 3547 (2002).
[36] Y. Yamamoto, K. Nakajima, T. Ohsawa, Y. Matsumoto, and H. Koinuma, Jpn. J. Appl. Phys. **44**, L511 (2005).
[37] S. Yadavalli, M. H. Yang, and C. P. Flynn, Phys. Rev. B **41**, 7961 (1990).
[38] M. H. Yang and C. P. Flynn, Phys. Rev. Lett. **62**, 2476 (1989).
[39] S. A. Chambers, T. T. Tran, and T. A. Hileman, J. Mater. Res. **9**, 2944 (1994).
[40] P. Chen, P. S. Kuttipillai, L. Wang, and R. R. Lunt, Sci. Rep. **7**, 40542 (2017).
[41] W. Pies and A. Weiss, in *Landolt-Börnstein: Numerical Data and Functional Relationships in Science and Technology, New Series, Group III : Crystal and Solid State Physics, Volume 7, Crystal Structure Data of Inorganic Compounds. Part b, Key Elements O, S, Se, Te*, edited by K. H. Hellwege and A. M. Hellwege (Springer-Verlag, Berlin Heidelberg New York, 1975), p. 69.
[42] W. A. Jesser, Mater. Sci. Eng. **4**, 279 (1969).
[43] E. S. Machlin and P. Chaudhari, in *Synthesis and Properties of Metastable Phases*, edited by E. S. Machlin and T. J. Rowland (The Metallurgical Society of AIME, Warrendale, 1980), p. 11–29.
[44] C. P. Flynn, Phys. Rev. Lett. **57**, 599 (1986).
[45] R. Bruinsma and A. Zangwill, J. Phys. (Paris) **47**, 2055 (1986).
[46] A. Zunger and D. M. Wood, J. Cryst. Growth **98**, 1 (1989).
[47] A. R. Kaul, O. Y. Gorbenko, and A. A. Kamenev, Russ. Chem. Rev. **73**, 861 (2004).
[48] A. Proessdorf, M. Niehle, M. Hanke, F. Grosse, V. Kaganer, O. Bierwagen, and A. Trampert, Appl. Phys. Lett. **105**, 021601 (2014).